To be submitted to JGR-Planets, 1999 **FINAL DRAFT - - Jan. 4, 1999**

THE DUST FLUX MONITOR INSTRUMENT (DFMI) FOR THE *STARDUST* MISSION TO COMET WILD-2

A.J. Tuzzolino[1], R.B. McKibben[1], J.A. Simpson[1], J.A.M. McDonnell[2], M.J. Burchell[2], B. Vaughan[2], P. Tsou[3], M.S. Hanner[3], B.C. Clark[4] and D.E. Brownlee[5]

[1]Laboratory for Astrophysics and Space Research, Enrico Fermi Institute, The University of Chicago, Chicago, IL 60637, USA

[2]Unit for Space Sciences and Astrophysics, School of Physical Sciences, University of Kent, Canterbury, Kent CT2 7NR, U.K.

[3]NASA Jet Propulsion Laboratory, 4800 Oak Grove Drive, Pasadena, CA 91109, USA

[4]Lockheed Martin Astronautics, P.O. Box 179, Denver, CO 80201, USA

[5]Department of Astronomy, University of Washington, Seattle, WA 98125, USA

ABSTRACT

The DUST FLUX MONITOR INSTRUMENT (DFMI) is part of the *STARDUST* instrument payload. The prime goal of the DFMI is to measure the particle flux, intensity profile, and mass distribution during passage through the coma of Comet Wild-2 in 2004. This information is valuable for assessment of spacecraft risk and health, and also for interpretation of the laboratory analysis of dust captured by the Aerogel dust collectors and returned to Earth. At the encounter speed of 6.1 km/s, the DFMI measurements will extend over the particle mass range of 8 decades, from 10^{-11} to $>10^{-3}$ g. A secondary science goal is to measure the particle flux and mass distribution during the ~ 7 year interplanetary portions of the mission, where, in addition to measurements of the background interplanetary dust over the radial range 0.98 AU to 2.7 AU, multiple opportunities exist for possible detection by the DFMI of interplanetary particles, meteor-stream particles, and interstellar dust. The DFMI consists of two different dust detector systems — a polyvinylidene fluoride (PVDF) DUST SENSOR UNIT (SU), which measures particles with mass $< \sim 10^{-4}$ g, and a DUAL ACOUSTIC SENSOR SYSTEM (DASS), which utilizes two quartz piezoelectric accelerometers mounted on the first two layers of the spacecraft Whipple dust shield to measure the flux of particles with mass $> 10^{-4}$ g. The large Whipple shield structures provide the large effective sensitive area required for detection of the expected low flux of high-mass particles.

1. INTRODUCTION

The principal goal of the *STARDUST* spacecraft is to collect and return to Earth cometary and interstellar dust particles captured in Aerogel capture cells. The spacecraft will fly through the coma of Comet Wild-2 in 2004, collecting dust particles, taking close-up images of the comet nucleus and coma, and gathering information on the coma particle spatial densities, mass distributions, and chemical composition. The DUST FLUX MONITOR INSTRUMENT (DFMI) will provide the real-time data on variations in the particle flux and mass distribution in the coma; the in-situ chemical composition data will be provided by the COMETARY AND

INTERSTELLAR DUST ANALYZER (CIDA) instrument. The *STARDUST* Mission characteristics, mission objectives, and science payload are described in detail in the accompanying papers (this issue) by Brownlee, et al., 1999, Tsou, et al. 1999, Kissel et. al., 1999, Newburn, et al. 1999, Anderson, et al. 1999 and Duxbury, et al. 1999.

Although a high rate dust sensor was not originally part of the *STARDUST* payload, a need for in-situ dust intensity and mass measurements was recognized during development of the mission. The concept originally considered called for use of sensors on the Whipple shield bumper to use the entire bumper as a dust flux monitor. However, because of several drawbacks (including signal characteristics) a more proven approach was adopted. Therefore, a DUST FLUX MONITOR INSTRUMENT (DFMI) patterned after a Cassini Mission instrument was adopted. The DFMI was originally configured to consist of a DUST SENSOR UNIT (SU), containing two polyvinylidene fluoride (PVDF) sensors, and an associated ELECTRONICS BOX (EB). To extend the range of measurement to high mass particles ($>10^{-4}$ g), which are expected to have a very low flux, the *STARDUST* project requested that the initial DFMI be expanded to include a DUAL ACOUSTIC SENSOR SYSTEM (DASS). The DASS consists of two acoustic sensors mounted to the first two layers of the large area dust shield which protects the spacecraft from large dust impacts..

With the addition of the DASS, the final flight DFMI consists of a PVDF dust SENSOR UNIT (SU), the two acoustic sensors (A1 and A2) of the DASS, and an ELECTRONICS BOX (EB). These components are shown in **Figure 1**. In **Figure 2**, the mounting positions of the SU and DASS sensors A1 and A2 are shown more clearly. The SU is mounted on the front of the first layer of the dust shield, which is a composite honeycomb structure known as the Bumper Shield. Detector A1 is mounted on the back of the Bumper Shield in the location shown. Detector A2 is mounted on the front of the second shield, a NEXTEL fabric layer to which is attached a thin carbon-fiber composite sheet, called the Acoustic Plate. The DFMI was designed, built and tested at the University of Chicago. The University of Chicago, which has extensive experience with PVDF systems, is primarily responsible for calibration of and analysis of data from the PVDF sensors. The DASS acoustic plate assembly and selection of flight-quality sensors was the responsibility of Lockheed Martin Astronautics, in Denver. The University of Kent, which has experience with acoustic detector systems, is principally responsible for calibration of and analysis of data from the DASS detectors.

The PVDF sensors in the DFMI will measure differential and cumulative particle fluxes over the particle mass range 10^{-11} - 10^{-4}g and cumulative particle fluxes for masses > 10^{-4}g. The acoustic sensors mounted on the spacecraft shield structures are intended to provide particle flux data for larger mass particles which, given the relatively small sensitive area (220 cm^2 total)of the PVDF sensors, would have fluxes too low to expect impacts on these detectors. By mounting the acoustic sensors to the much larger area Bumper panel (~ 0.7 m^2) and Acoustic plate (~ 0.5 m^2), the area factor for detection of the larger particles is greatly increased. One acoustic sensor (A1) will detect large particles that impact the Bumper panel. The other acoustic sensor (A2) will detect only those particles with sufficiently higher mass to penetrate the Bumper panel and impact the Acoustic plate (see **Figure 1**). While the sensitive area for these detectors is essentially the

area of the shield panels, and thus much larger than the PVDF area, because of the uncertainty of the impact location with respect to the DASS sensors, the information concerning particle mass available from the DASS sensors will be much less accurate than that for smaller particles from the PVDF sensors.

In this paper, we give a detailed description of the DFMI sensor systems and the DFMI operational modes, data formats, data acquisition, dust particle calibrations, and anticipated data after launch.

2. OBJECTIVES OF THE DFMI

2.1 Comet Flyby

The prime scientific objective of the DFMI is to carry out quantitative measurements of particle impact rate and particle mass distribution throughout the flyby of Comet Wild-2. The DFMI data are fundamental for establishing the physical processes of dust emission from the nucleus, their propagation to form a coma, and the behavior of dust jets. During the several hours of flight through the coma, the particle mass range covered by the PVDF sensors at the 6.1 km/s impact velocity (at comet flyby) ranges from 10^{-11} to 10^{-4} g for differential and cumulative flux measurements and > 10^{-4} g for cumulative flux measurements. As discussed below, the sensitivity of the DASS detectors is expected to overlap the mass range of the PVDF detectors by more than one order of magnitude, thus providing intercalibration to help in extending the dust spectrum to larger masses.

The high counting rate capability of the DFMI PVDF sensors (SECTION 4) is more than sufficient to obtain accurate instantaneous fluxes throughout the Wild-2 flyby. Thus any jets from the Wild-2 nucleus should be easily measured. During the flyby, the DFMI will provide measurements of the dust flux at least once per second, and up to 10 times per second, depending on the dust particle flux. Further, since the counters do not reset upon readout, accurate cumulative particle fluences will be obtained, even over data gaps. These in-situ data will be important for correlation with the in-situ measurements of the CIDA instrument (Kissel et al., 1998), as well as for correlation with the size distribution data obtained from the cometary particles returned to Earth in the Aerogel capture cells.

The dust data from the combined DFMI PVDF and acoustic sensors during the encounter will cover a very wide mass range from ~10^{-11} g up to several g, while the CIDA instrument will extend the range downward to as low as 10^{-16} g. In addition to its scientific importance, this wide mass range and the high time resolution (100 ms/readout) of the measurements will provide important information on the dust environment relevant to engineering concerns for spacecraft health and interpretation of anomalies.

2.2 Cruise

During interplanetary cruise, a further science objective of the DFMI is to provide additional observations to help characterize the interplanetary dust complex and, in particular, to search for evidence of detection of meteor stream particles and, possibly, of the interstellar dust stream. Because of the very low flux of large particles expected from these sources and the risk of acoustic signals generated as a result of routine spacecraft operations (see Section 4.1), only events registered in the PVDF sensors will trigger generation of data packets during interplanetary cruise (see Section 3). The three loops of the spacecraft about the Sun over the approximately seven year duration of the *STARDUST* mission provide for multiple near approaches of the spacecraft to known meteor streams and for several opportunities for interstellar dust detection (SECTION 8.1).

3. THE DUST FLUX MONITOR INSTRUMENT (DFMI)

The PVDF portion of the DFMI has significant inheritance from the University of Chicago DUST COUNTER AND MASS ANALYZER instrument (DUCMA) flown earlier on the *Vega-1* and *Vega-2* spacecraft to Comet Halley (Simpson et al., 1986) and from the University of Chicago HIGH RATE DETECTOR (HRD) recently launched on the *CASSINI* spacecraft to Saturn (Tuzzolino, 1996; Tuzzolino, 1998).

The detectors in the DFMI SENSOR UNIT (SU), shown in **Figures 1** and **2**, employ the polyvinylidene fluoride (PVDF) dust particle detection technique described by Simpson and Tuzzolino (1985). The large PVDF sensor has a sensitive area of 200 cm^2 and a thickness of 28μm. The small PVDF sensor has a sensitive area of 20 cm^2 and a thickness of 6μm. The SU is rigidly mounted to the spacecraft Bumper panel and is connected to the DFMI ELECTRONICS BOX (EB), which is mounted within the spacecraft body, by a ~1.5m long cable. The acoustic sensors are mounted to the Bumper panel and Acoustic plate, as shown in **Figures 1** and **2**, and each acoustic sensor is connected to the EB by means of a ~ 2.4m long cable.

There are three operating modes for the DFMI:

a) **CRUISE MODE:** Continuous recording by the PVDF and acoustic sensors of particle impacts for each of the eight PVDF sensor thresholds and the four acoustic sensor thresholds (SECTIONS 6.1 and 6.2).

   During cruise mode operation of the DFMI, the DFMI software samples the accumulated counts corresponding to the lowest thresholds of the large and small PVDF sensors every 100 ms. If (and only if) there is a change in either of the accumulated counts in a 100 ms interval, the DFMI transmits a **DFMI DATA PACKET** (SECTION 6.2) to the spacecraft **COMMAND AND DATA HANDLING (C&DH)** system for storage. Thus in cruise mode the maximum time resolution for counting rates is 100 ms, but no data are generated if no events are registered in the PVDF detectors.

b) **ENCOUNTER MODE:** This mode is identical to **CRUISE MODE** except that a DFMI data packet will automatically be sent to the spacecraft once per second even if no PVDF sensor events have occurred during a 1s interval. Thus counting rate time resolution can vary from 1s to 100ms, and, even if the PVDF sensors were to fail, data from the DASS detectors will be sampled and returned once per second.

c) **CALIBRATE MODE:** Periodic (~ once per month) electronic calibration of the DFMI with the DFMI **IN-FLIGHT CALIBRATOR (IFC)**. The IFC sends a sequence of 1024 pulses of various known amplitudes to the PVDF sensor electronics. This allows assessment of the electronic stability of the DFMI PVDF sensor system electronics throughout the interplanetary mission.

4. PVDF DUST SENSORS

The theory, fabrication and details of PVDF dust detector operation have been described in earlier reports (Simpson and Tuzzolino, 1985; Perkins, Simpson and Tuzzolino, 1985; Simpson, Rabinowitch and Tuzzolino, 1989). A PVDF sensor (**Figure 3a**) consists of a thin film of permanently polarized material, whose polarization vector is normal to the film surface. A hypervelocity dust particle impacting the sensor produces rapid local destruction of dipoles (either a crater or a penetration hole) which results in a large and fast (ns range) current pulse at the input to the electronics. The output pulse from the linear electronics (**Figures 3b - 3e**) is sharp in time, with a maximum amplitude depending on impacting particle mass and velocity (SECTION 7).

Since the depolarization induced current pulse is fast (ns range), the choice of electronic time constants for the preamplifiers and shapers determines the output pulse shape. Electronic time constants (amplifier shaping time constants, discriminator width) in the few microsecond range permit a high counting rate capability for the DFMI PVDF sensor-electronics combination (10^4 random impacts s^{-1} with <5% corrections), as illustrated in **Figure 3f**. The high counting rate capability of the DFMI PVDF sensor system is of particular importance for the Wild-2 flyby measurements, where high dust particle fluxes may be encountered.

4.1 PVDF Sensor Acoustic Signal Suppression

As discussed in earlier reports (Simpson and Tuzzolino, 1985; Perkins, Simpson and Tuzzolino, 1985), PVDF detectors have a secondary but minor mode of response due to their piezoelectric properties. Therefore, background acoustic disturbances of sufficient intensity could trigger the DFMI PVDF detector thresholds and lead to generation of data packets, which could be mistakenly interpreted as originating from dust particle impacts. During the *STARDUST* mission, possible sources of acoustic disturbances include spacecraft gas jets, moving mechanisms, and large particle impacts on the Bumper panel near the mounting positions of the DFMI PVDF sensors.

To minimize the effects of these possible acoustic backgrounds, the DFMI PVDF sensors are mounted in vibration absorbing pads (**Figure** 4). This design was highly effective in suppressing the acoustic response from mechanical shocks during the VEGA missions to comet Halley (Perkins, Simpson and Tuzzolino, 1985). During the STARDUST mission, additional protection will be provided by the good time resolution of the measurements, allowing correlation with known spacecraft events, and by the presence of the acoustic sensors of the DASS system, which in general should not be triggered by true dust particle impacts on the DFMI SU detectors.

4.2 PVDF Dust Sensor Thermal Control

Thermal control of the DFMI PVDF dust sensors in flight is challenging because the sensors at various times during the mission may view both full sun and black space. At the same time, there is no significant conductive path coupling the thin foil sensors to heat sources or sinks, so that without control, wide temperature excursions would be expected for the detectors. Under full sun conditions, the uncontrolled temperatures could rise to levels that would destroy the detectors. In the absence of conductive paths, control must be provided by efficient radiative coupling between the dust sensors and the heated SU bottom plate (**Figure 5a**). To accomplish this, a spacecraft-powered heater element located on the underside of the bottom plate of the SU maintains the bottom plate at temperature T_o. The back face of the sensor is coated with CHEMGLAZE (Z-306) black paint and views a Z-306 coating which is applied to that portion of the plate facing the coated sensor surface. **Figures 5b-5d** show calculated sensor temperature vs. assumed plate temperature for full solar illumination at 1.0 and 2.0 AU (panels "b" and "c") and for the case of no solar illumination (panel "d") for an assumed value of the thermal emissivity $\varepsilon_2 = 0.84$ for the ChemGlaze coating on the detectors and bottom plate.

Operating temperature limits for the PVDF sensors are -50°C to +50°C. The data in **Figure 5** show that with the assumed value of ε_2 the sensor temperature T will remain within the operating temperature limits if the SU mounting plate temperature T_o is maintained within the temperature range $-50°C \leq T_o \leq 20°C$. For non-operating conditions, temperature limits for the PVDF sensors are -65°C to +65°C and values of T_o in the range $-65°C \leq T_o \leq 50°C$ (**Figure 5**) would be required to satisfy the non-operating temperature limits.

The value $\varepsilon_2 = 0.84$ required for the detector coating can be achieved by applying a suitable thickness of the ChemGlaze Z-306 coating to the detector surface using a spray brush. Measured values of ε_2 vs. Z-306 thickness are plotted in **Figure 6a**. For the PVDF sensors on *STARDUST* a Z-306 thickness of ~ 30 μm has been used, yielding a measured value $\varepsilon_2 = 0.84$. The coated PVDF sensors have been thermally cycled over the temperature range -200°C to 115°C and the coatings have shown excellent adherence to the PVDF surface and complete mechanical stability. Coated sensors have also successfully survived the required simulated launch vibration and shock environments (random vibration up to 55 g rms, shock acceleration with peak acceleration of 1750 g). Extensive dust particle calibrations of 6 μm thick and 28 μm thick PVDF sensors having no coating, as well as sensors having 30 μm thick ChemGlaze coatings on the back surface showed that the particle responses were identical for coated and uncoated sensors. (Section 7)

4.3 Temperature Dependence of PVDF Sensor Dust Particle Output Signal

During the *STARDUST* mission, the extreme temperatures for the PVDF sensors are assumed here to be in the range - 50°C to + 50°C. For dust particles of fixed mass and velocity impacting a PVDF sensor, two temperature dependent parameters determine the variation of output signals from the sensor-linear electronics combination as the temperature of the PVDF sensor changes:

1) the variation in sensor capacitance with temperature, and;

2) the variation of the dust particle depolarization induced charge signal with temperature.

These two contributions are discussed below

4.4 PVDF Detector Capacitance And Amplifier Design

The two PVDF sensors have capacitances of ~ 68 nF (200 cm^2, 28μm thick) and ~25 nF (20 cm^2, 6 μm thick) at room temperature. **Figure 6b** shows the measured dependence of PVDF sensor capacitance on temperature. Over the expected temperature range for the DFMI PVDF sensors during the mission (-50°C to +50°C), **Figure 6b** establishes the range of sensor capacitance which the pre-amplifier must accommodate. The final design of the sensor pre-amplifier was such that variations in sensor capacitance over the temperature range -50°C to +50°C produced variations in the pre-amplifier pulse height (stimulated by an electronic pulser) of less than 2%.

The large PVDF sensor capacitance also had to be considered in the design of the linear electronics with respect to the counting rate requirements we imposed for the *STARDUST* mission. A high counting rate capability, up to 10^4 random impacts s^{-1} per sensor with <5% dead-time corrections, was imposed to allow for the large uncertainty in the maximum particle counting rates to be expected during comet flyby. This requirement was satisfied by using 2μs time constants for the post amplifier pulse shaping and a discriminator width of 4 μs (SECTION 6.1) for the final flight electronics.

To determine an optimum choice for the small PVDF sensor's lowest mass threshold, the electronic noise (FWHM) for the combination sensor, preamplifier (CSA) and shaping amplifier must be considered. If the lowest mass threshold is set too low, electronic noise counts will contribute to the total measured counts. If it is set too high, low-mass particles are lost.

The measured electronic noise (FWHM) for the PVDF sensor linear electronics vs. capacitance at the CSA input is shown in **Figure 6c**. For the small sensor the FWHM electronic noise is ~4.0×10^5 e (electron charge units)or 1.7×10^5 e (rms). By setting the lowest electronic threshold for the small PVDF sensor at 3.8×10^6 e (e.g., a factor 22.4 above the rms noise), electronic noise counts are completely excluded (see **Table 4**).

4.5 PVDF Detector Charge Signal

Of the several PVDF material parameters which determine the magnitude of the PVDF detector depolarization charge signal resulting from an impacting dust particle (Simpson and Tuzzolino, 1985), the volume polarization magnitude, P, and its temperature dependence are the most important for determining the temperature dependence of the signal amplitude. Our laboratory measurements have shown that over the temperature range -50 to + 80°C, the charge signal amplitude will vary by less than 6% from the values measured at room temperature. Thus, we expect an overall possible variation in output signal amplitude resulting from both detector capacitance and depolarization charge signal temperature effects of less than 10% over the expected temperature range for the detector. This maximum 10% effect will contribute a negligible uncertainty for the particle mass thresholds.

5.0 ACOUSTIC SENSORS

The DFMI utilizes two commercially available quartz piezoelectric acoustic sensors mounted to the spacecraft Bumper panel and Acoustic plate, as illustrated in **Figures 1** and **2**. The sensors (model No. J351B31) were obtained from PCB Piezotronics, Inc., Depew, NY. According to the supplier's specifications these sensors operate over the temperature range -200°C to 121°C and have a <20% variation in signal amplitude over this entire temperature range. Each sensor is housed in a can, which also contains a stage of linear electronics. For the flight electronics, the acoustic sensor outputs were fed to additional electronics, which provided a signal gain of a factor 20.

Sensor A1 is attached to the underside of the Bumper panel and will respond to large-mass particles that impact the Bumper panel. Sensor A2 is attached to the upper surface of the Acoustic plate and will respond only to those large mass particles which penetrate the Bumper panel. Both fragments of the incident particle and fragments of the Bumper panel generated during penetration contribute to the A2 response.

The signal wave shape from the acoustic sensor-electronics combination that results from a particle impact consists of a complex sinusoidal, long duration signal which eventually decays to zero (see SECTION 8). The wave shapes and amplitudes for a given particle impact velocity will depend on particle mass and on the position of the impact with respect to the location of the acoustic sensor mounted on the Bumper panel or Acoustic plate. To illustrate the nature of the response from the DFMI acoustic sensors, we have simulated a high-velocity (6.1 km/s) impact on the Bumper panel of a milligram-sized particle by dropping gram sized aluminum spheres onto the Bumper panel from a known height (**Figure 7a**). In **Figures 7b** and **7c** we show examples of the output signals from an acoustic sensor for two different impact points on the Bumper panel for impacts by an 0.47 g aluminum sphere.

Each of the two acoustic sensors has two electronic thresholds — a low threshold called "**a**", and a high threshold called "**b**". The "**a**" and "**b**", thresholds for A1 are identical to those for A2. The discriminator output for threshold **a** has a time width $T_1 = 510\mu s$, and that for **b** a time width $T_2 = 210\ \mu s$.

To illustrate how the number of counts registered by the **a** and **b** discriminators for a single particle impact can provide an estimate of impacting particle momentum, we use the results discussed in SECTION 8 and assume here a greatly simplified form for the output signal from an acoustic sensor. Assume a particle of momentum P_0 impacts the Bumper panel at time $t = 0$ and that the acoustic sensor signal $V(t)$ resulting from the impact is given by the damped harmonic oscillator expression

$$V(t) = G[P_0]^{\lambda}\, e^{-t/\tau} \cos\left(\frac{2\pi}{\Delta t} t\right), \tag{1}$$

where G is a constant, λ is a momentum exponent, τ is the decay time of the output pulse train, and Δt is the time interval between successive positive maxima (or negative minima) in the pulse train. The values for G and λ depend on whether the particle momentum is less than, or greater than, the ballistic limit for the Bumper (SECTION 8). For $\tau >> \Delta t$, the envelope of the positive maxima $V_e(t)$ is given by

$$V_e(t) = V_o\, e^{-t/\tau}, \tag{2}$$

where $V_o = G[P_0]^{\lambda}$.

If a discriminator is set at a voltage level V_1, then the time t_1 at which $V_e(t_1) = v_1$ is given by

$$V_1 = V_o\, e^{-t_1/\tau}, \tag{3}$$

or

$$t_1 = \tau \ln\left(\frac{V_o}{V_1}\right). \tag{4}$$

For a second discriminator set at a level V_2, where $V_2 > V_1$, an identical argument gives

$$t_2 = \tau \ln\left(\frac{V_o}{V_2}\right). \tag{5}$$

If N_1 and N_2 are the number of recorded counts corresponding to the thresholds V_1 and V_2, then

$$N_1 = 1 + \frac{t_1}{T_1} = 1 + \left(\frac{\tau}{T_1}\right) \ln\left(\frac{V_0}{V_1}\right), \tag{6a}$$

$$N_2 = 1 + \frac{t_2}{T_2} = 1 + \left(\frac{\tau}{T_2}\right) \ln\left(\frac{V_0}{V_2}\right). \tag{6b}$$

If N_1 and N_2 are measured, V_o is determined from Eq. (6a,b). In **Figure 7d**, N_1 and N_2 are calculated from Eq. (6a,b)

6.0 DFMI ELECTRONICS, DIGITAL DATA AND COMMANDS

Figure 8a shows a block diagram of the principal electronic functions of the DFMI, showing the two independent dust sensor systems — the PVDF DUST SENSOR UNIT (SU), and the DUAL ACOUSTIC SENSOR SYSTEM (DASS). **Figure 8b** shows a schematic of the DFMI electrical interface to the spacecraft.

6.1 Linear (Analog) Electronics

The DFMI linear electronics for the PVDF sensors consists of charge sensitive preamplifiers (CSA), shaping amplifiers (SHAPER) and threshold discriminators. Each SHAPER provides single integration - single differentiation RC shaping with a shaping time constant of 2μs. A particle impact on either the large or small PVDF sensor will result in output signals (**Figures 3b - 3e**) from the shapers which may trigger the M1, M2, M3, M4 thresholds for the large PVDF sensor, or the m1, m2, m3, m4 thresholds for the small PVDF sensor. As a contingency, the m1- m4 electronic thresholds may be increased by a fixed factor (~ factor 10) by ground command, which would activate a mass THRESHOLD SWITCH for the small sensor (**Figure 8a**).

The DFMI linear electronics for each of the acoustic sensors consists of a wide-band amplifier which increases the output signal from the acoustic sensor internal amplifier by a factor 20. This amplified signal feeds discriminators set at 0.1 volts and 1.0 volts, respectively. Each of the discriminators feed a ONE SHOT having a time width of 0.5 ms (T_1) and 0.2 ms (T_2), respectively.

6.2 Digital Electronics and Data

Each of the PVDF sensor discriminator outputs M1-M4, and m1-m4, will increment a 16 bit counter, and each of the acoustic sensor ONE SHOT outputs, A1a, A1b, A2a, and A2b, will increment 8-bit counters. The basic DFMI data packet consists of 12-16 bit words as listed in **Table 1.** To this basic DFMI data packet, the spacecraft data handling system appends the S/C clock, S/C attitude, position and velocity and DFMI EB and SU temperatures.

6.3 DFMI Commands

The commands passed to the DFMI from the spacecraft are shown in **Table 2.** The DFMI calibrate command will be issued about once each month to assess DFMI electronic stability. The DFMI **SENS. THRESH ON** command raises the small detector thresholds by a factor ~10 and is a contingency command only, to be used, for example, in case of a noisy m1 channel.

Table 1

16 BIT WORD	BYTE NUMBER LSB MSB
SYST	Byte 1 and 2
CLK	Byte 3 and 4
A1a, A1b	Byte 5 and 6
A2a, A2b	Byte 7 and 8
M1	Byte 9 and 10
M2	Byte 11 and 12
M3	Byte 13 and 14
M4	Byte 15 and 16
m1	Byte 17 and 18
m2	Byte 19 and 20
m3	Byte 21 and 22
m4	Byte 23 and 24

SYST: Byte 1 contains the DFMI status and Byte 2 is the fixed DFMI sync pattern (A5 hex = 165 decimal)

CLK: Bytes 3 and 4 contain the 16 bit roll over seconds DFMI counter

A1a,A1b: Bytes 5 and 6 contain the two 8 bit counters for the two thresholds for the BUMPER acoustic sensor. Byte 5 is the lowest threshold

A2a, A2b: Bytes 7 and 8 contain the two 8 bit counters for the two thresholds for the NEXTEL (Acoustic Plate) acoustic sensor. Byte 7 is the lowest threshold

M1: Bytes 9 and 10 contain the running sum of the 16 bit counter for the 1st (lowest) large sensor threshold M1.

M2: Bytes 11 and 12 contain the running sum of the 16 bit counter for the 2nd large sensor threshold M2.

M3: Bytes 13 and 14 contain the running sum of the 16 bit counter for the 3rd large sensor threshold M3.

M4: Bytes 15 and 16 contain the running sum of the 16 bit counter for the 4th large sensor threshold M4

m1: Bytes 17 and 18 contain the running sum of the 16 bit counter for the 1st (lowest) small sensor threshold m1.

m2: Bytes 19 and 20 contain the running sum of the 16 bit counter for the 2nd small sensor threshold m2.

m3: Bytes 21 and 22 contain the running sum of the 16 bit counter for the 3rd small sensor threshold m3.

m4: Bytes 23 and 24 contain the running sum of the 16 bit counter for the 4th small sensor threshold m4.

Table 2

DFMI Command List

Command MSB LSB	Function
DFMI_Start_Readout	Enables DFMI Data Transmission
DFMI_Stop_Readout	Disable DFMI Data Transmission
DFMI_Cruise_Mode	Sets DFMI to Cruise Mode
DFMI_Encounter Mode	Sets DFMI to Encounter Mode
DFMI_Calibrate	Sets DFMI to Calibrate Mode
DFMI_Sens_Thresh On* (PVDF)	Sets Small Sensor Relay to On
DFMI_Sens_Thresh Off (PVDF)	Sets Small Sensor Relay to Off

* DFMI_Sens_Thresh On: Sets the small detector sensitivity levels a factor 10 higher to measure larger mass particles

7.0 PVDF SENSOR CALIBRATIONS

Particle calibrations of DFMI-type PVDF sensors (28μm and 6μm thick) were carried out by the University of Chicago group at the Heidelberg and Munich dust accelerator facilities, as summarized

Particle calibrations of DFMI-type PVDF sensors (28μm and 6μm thick) were carried out by the University of Chicago group at the Heidelberg and Munich dust accelerator facilities, as summarized in **Table 3** (Simpson and Tuzzolino, 1985; Simpson, Rabinowitch, and Tuzzolino, 1989). The characteristics of the Heidelberg and Munich accelerators are such that the highest particle mass we could measure at the Heidelberg facility was $\sim 1.8 \times 10^{-10}$ g, and the lowest particles mass we could measure from the Munich facility was $\sim 4 \times 10^{-9}$ g. Thus, we have no calibration data for particles in the mass range between $\sim 1.8 \times 10^{-10}$ g and $\sim 4 \times 10^{-9}$ g for either the 6μm thick or the 28 μm thick PVDF sensors.

Over the mass intervals where we have calibration data, fits to the calibration data have been obtained which show that the PVDF sensor signal amplitude, in units of number of electron charges (e), is proportional to $\mathbf{m^a v^b}$, where **m** and **v** are particle mass and velocity, and **a** and **b** are exponents derived from the calibration data. In **Figure 9**, we show calculated PVDF sensor output signal vs impacting particle mass, m (g), for impacts at the flyby encounter velocity of 6.1 km/s, based on our calibration data. From these data, and our selected electronic thresholds for the PVDF sensors, we obtain the particle mass thresholds given in **Table 4**. For impacts at other impact velocities (i.e., impacts by interplanetary or meteor stream particles), different sets of mass thresholds are obtained.

Additional calibration data, which includes particles over the mass range not yet covered, will be required to obtain complete, definitive calibrations for the 6 and 28 μm thick PVDF sensors. These additional data will clarify possible discrepancies between the Heidelberg and Munich results so far obtained (cf. **Figure 1**, where extrapolation to low masses of the trend defined by the Munich data appears inconsistent with the high mass measurements from the Heidelberg data, especially for the 6 μm thick sensor).

Table 3

Summary of PVDF Dust Sensor Calibrations

Heidelberg: August 1983 June 1984 January 1994 **Munich:** October 1987 April 1989 January 1994	**6 μm**	**28 μm**
1. MPI-K Heidelberg (Fe Particles)		
a) Velocity Range (km/s)	1.0 - 12.0	1.7 - 11.4
b) Mass Range (g)	3.8×10^{-13} - 1.7×10^{-10}	2.8×10^{-13} - 1.9×10^{-10}
c) Diameter Range (μm)	0.45 - 3.3	0.40 - 3.4
2. Munich/Garching (Glass Particles)		
a) Velocity Range (km/s)	1.8 - 15.9	2.0 - 11.4
b) Mass Range (g)	2.4×10^{-9} - 2.0×10^{-6}	5.4×10^{-9} - 3.0 10^{-6}
c) Diameter Range (μm)	12 - 115	16 - 130
3. Range of Measured Sensor Signal Amplitudes (In Units of Number of electron charges, e)		
a) Smallest	8.3×10^{4} e (Fe)	2.7×10^{4} e (Fe)
b) Largest	8.5×10^{9} e (Glass)	4.2×10^{10} e (Glass)

Table 4

Dust Flux Monitor Instrument (DFMI) Flight Unit

(Electronic Thresholds and Corresponding Particle Mass Thresholds for 6.1 km/s Impact Velocity)

Large PVDF Sensor Area = 200 cm² Thickness = 28 μm			**Small PVDF Sensor Area = 20 cm² Thickness = 6 μm**		
Electronic Threshold +	**Particle Mass Threshold**	**Particle Diameter ***	**Electronic Threshold**	**Particle Mass Threshold**	**Particle Diameter ***
1.76 X 10^9 e	8.5 x 10^{-8} g	55 μm	3.77 x 10^6 e	9.8 x 10^{-12} g	2.7 μm
			7.13 x 10^7 e	1.2 10^{-10} g	6.1 μm
2.67 x 10^{10} e	1.7 x 10^{-6} g	148 μm	1.8 x 10^8 e	4.3 x 10^{-9}	20.2 μm
			6.0 x 10^9 e	6.3 x 10^{-7} g	106 μm
2.67 x 10^{11} e	1.4 x 10^{-5} g	299 μm	**Ground Command Electronic Threshold**	**Ground Command Particle Mass Threshold**	**Ground Command Particle Diameter**
			4.6 x 10^7 e	7.0 x 10^{-11} g	5.1 μm
2.0 x 10^{12} e	1.5 x 10^{-4} g	659 μm	8.7 x 10^8 e	2.6 x 10^{-8} g	36.8 μm
			2.2 x 10^9 e	1.2 x 10^{-7} g	61 μm
			7.3 x 10^{10} e	1.7 x 10^{-5} g	319 μm

* Assuming impacting particle with density 1.0 g/cm^3
\+ Electronic thresholds in units of number of electron charges (e)

8.0 ACOUSTIC SENSOR CALIBRATIONS

The use of acoustic sensors for impact detection of small particles in space was first proposed many years ago (e.g. McDonnell, 1969, and McDonnell and Abellanas, 1972). Such a system was used on the Giotto spacecraft, which visited comet Halley and determined the dust density and mass distribution near the comet (McDonnell *et al.*, 1986). The DFMI sensor mounted on the bumpershield has been extensively tested at the Hypervelocity Impact Laboratory of the University of Kent (Burchell *et al.*, 1999) and a preliminary report is given in McDonnell et al. 1999. This has been achieved by a series of shots on a two-stage light gas gun (LGG), combined with bead drop tests. The former permits determination of the ballistic limit of the shield and provides example output from the sensor mounted on the shield. The latter allows a detailed investigation of the attenuation properties of the wave propagation from the impact point to the sensor.

8.1 Bumpershield Ballistic Limit

The LGG can be fired at the STARDUST encounter velocity of 6.1 km s^{-1}, and both the size and composition of the projectile can be chosen. Most projectiles used in this work were spheres of diameter in the range 1 to 2 mm, and their impacts resulted in penetration of the rear surface of the bumpershield (i.e., exceeded the ballistic limit). The velocity used in the majority of the shots was slightly lower than the 6.1 km s^{-1} encounter speed, to permit acquisition of more data on the ballistic limit region. The types of projectile used were soda lime glass and aluminum. The velocity (measured in each shot to better than 1% accuracy) and projectile size ranges are given in **Table 5.**

Table 5
Velocity and size range of projectiles used in the Light Gas Gun Shot Program

Projectile	Velocity (km s^{-1})	Diameter (mm)
Soda lime glass	5.29 - 6.10	0.195 – 1.05
Aluminum	4.69 - 5.75	0.80 – 1.50

For each shot a 10 cm x 10 cm tile of bumpershield material was placed in the target chamber of the LGG. To determine the ballistic limit, measurement of the area of the exit hole was made. For the aluminum and glass shots, the resulting exit hole is shown vs. impact momentum in **Figure 10.** Incident momentum was chosen because the amplitude of the signal acquired by the accelerometer is proportional to this parameter. There is a non-linear dependence of the exit hole area on momentum; no perforation is found at 5 x 10^{-5} N s, marginal perforation is found at 5 x 10^{-4} N s, and a sharp rise in exit hole area is seen at 5 – 10 x 10^{-3} N s. The data are fit by a function of the form

$$Y = A + (B - A)/(1 + e^{(x - C)/D*x)}),$$

and it was found that A=41.2, B= -42.6, c = -215.2, and D = 1.12, with a regression coefficient of 0.97. No significant difference is seen between the data for glass and aluminum projectiles.

8.2 Acoustic Sensor Sensitivity as a Function of Impact Momentum

During the hypervelocity impact (HVI) tests an acoustic sensor (of the same type as the flight sensor) was attached to the tile midway along one side and 2 cm in from the edge of the tile. The sensor was powered with the same circuit as the flight sensors, but conditioning of the output signal did not include the amplification that occurs in the flight electronics. Note that all data in **Sections 8.2** and **8.3** are presented as obtained in this scheme with no subsequent amplification. The resulting signal was monitored on a digital storage oscilloscope and stored for subsequent analysis. An example signal (impact of a 1.0 mm diameter glass sphere at 6.1 km s^{-1}) is shown in **Figure 11.**

During each impact the acoustic sensor was read out and the peak response recorded. The impacts were located on the bumpershield 4.0 ± 0.5 cm from the center of the acoustic sensor. The magnitude of the peak signal from the acoustic sensor is shown vs. impact momentum in **Figure 12**. Also shown on **Figure 12** are data obtained from bead drop tests using a tile of bumpershield material of the same dimensions as those used in the HVI tests. Again the impacts were 4.0 ± 0.5 cm from the center of the acoustic sensor. The beads used were 1.0 and 1.5 mm diameter spheres of aluminum, stainless steel and tungsten carbide, dropped from heights of 30, 50, 100, 150, and 200 mm. Each drop was repeated 10 times and the averages are shown in **Figure 12**. The data in **Figure 12** show that there is a power law relation of the signal strength (S) to momentum (P) up to the ballistic limit. A fit to the data below the ballistic limit (approximately 3.0 x 10^{-4} N s) gives $S = 414000 \times P^{1.39}$ (where S is in V and P in N s), with a regression coefficient of 0.67. The difference in behavior in the two regimes is large, and reflects loss of containment of the event above the ballistic limit.

8.3 Attenuation of Signal by Transmission across the Bumpershield

As well as the relation of signal strength to impact momentum for impacts on the bumpershield at a fixed distance from the sensor, the attenuation of the signal strength has been measured as the impact location varies. For this a full size mock-up of the bumpershield was used, with the acoustic sensor placed as on the flight model (see **Figure 7a**). Bead drops were carried out, using 1.5 mm diameter (stainless steel) beads dropped from a height of 15 cm (again each drop was repeated 10 times). Drops were carried out every 1 cm along X and Y axes centered on the acoustic sensor position (axes directions defined as in **Figure 7a**).

The averaged maximum amplitudes of the resulting signals are shown in **Figure 13**. The signals along the +ve and –ve X axes are indistinguishable for equal distances of the impact location from the sensor. The data for X displacement are fit and it is found that the signal (S in Volts) varies with X (displacement in cm) according to $S = 1.433|X|^{-0.839}$, with a regression coefficient of 0.94. However, along the Y axis, the signal strength depends on whether the displacement is along the +ve or -ve Y axis. For +ve Y displacements the signal strength varies as $S = 2.69Y^{-0.657}$, regression coefficient = 0.96, whereas for –ve Y displacements the dependence is best described by $S = 1.766 - 0.0758|Y| + 0.000971|Y|^2$, regression coefficient 0.97. Power law fits to the data are significantly less satisfactory. This difference between +ve and –ve Y axis behavior seems to be intrinsic to the bumpershield, reflecting structure in its composition.

The combination of HVI and bead drop testing has permitted the sensitivity of the bumpershield and acoustic sensor to be measured. This can be combined with the response of the electronics readout to permit an estimate of the detector effective area as a function of impactor mass. This is necessary because during the encounter there is no means of determining the actual location of an impact. When combined with cometary dust emission modeling, the detector count rates can be predicted for various comet encounter flyby scenarios. A preliminary such analysis is reported by McDonnell *et al.* 1999.

9.0 POST LAUNCH DFMI OPERATIONS AND ANTICIPATED RESULTS

9.1 Cruise

Assuming that the DFMI will be powered for nearly all of the *STARDUST* mission, the *STARDUST* mission profile provides multiple opportunities for possible detection by the PVDF sensors of meteor stream particles (G. deNolfo, et al., 1991; Singer and Stanley, 1980) and interstellar particles (Grün, et al., 1993). For the case of meteor stream particles, our criteria for possible detection are:

a) the *STARDUST* trajectory must intersect the meteor stream orbit within a distance ~ 0.2 AU, and;

b) the relative velocity vector makes an angle of $\leq 45°$ with the normal to the PVDF sensors.

Item "b)" assumes that the spacecraft will provide the required spacecraft attitude. In **Figure 14a** we show the minimum STARDUST-stream separation for the Orionids meteor stream over the duration of the STARDUST mission. We see that during the mission six opportunities exist for possible detection of stream particles by the DFMI PVDF sensors. In **Figure 14b**, we show the trajectories of two selected meteor streams from a number of streams we have considered (Cook, 1973). For the ε-Geminids and Orionids streams, detection opportunities exist during each of the three spacecraft loops. In **Table 6**, we show the minimum spacecraft-meteor stream separations, and the approximate times ($\pm$ 10 days) at which they are expected to occur, for four selected meteor streams.

For the case of interstellar particles, the small flux expected (Grün et al., 1993) may preclude detection by the small area (20 cm^2) PVDF sensor.

Table 6

Minimum Spacecraft - Meteor Stream Separations for Four Selected Streams During Each of the Three Spacecraft Loops About the Sun

SELECTED METEOR STREAMS

Meteor Stream	Orbital Elements					
	a(AU)	e	q (AU)	ω (°)	Ω (°)	i (°)
Orionids	15.1	0.962	0.57	82.5	28.0	163.9
ε-Geminids	26.77	0.97	0.80	237	209	173
Leonids	11.5	0.915	0.98	172.5	234.5	162.6
Geminids	1.36	0.896	0.14	324.3	261.0	23.6

First Loop (Feb. 10, 1999 - Jan. 15, 2001)			Second Loop (Jan. 15, 2001 – Jul. 24, 2003)			Third Loop (Jul. 24, 2003 - Jan. 14, 2006)		
Date	Stream	Minimum Separation (AU)	Date	Stream	Minimum Separation (AU)	Date	Stream	Minimum Separation (AU)
Apr. 16,1999	Orionids	0.038	Apr. 19, 2001	Orionids	0.13	Oct. 24, 2003	Orionids	0.14
Jun. 10, 1999	ε-Geminids	0.12	Jun. 30, 2001	ε-Geminids	0.21	Dec.31, 2003	ε-Geminids	0.22
Oct. 25, 2000	Orionids	0.12	May 15, 2003	Orionids	0.05	Oct. 31, 2005	Orionids	0.05
Nov. 6, 2000	ε-Geminids	0.085	May 10, 2003	ε-Geminids	0.20	Nov. 5, 2005	ε-Geminids	0.12
Dec. 11, 2000	Germinids	0.034	Jun. 14, 2003	Leonids	0.16	Dec. 5, 2005	Leonids	0.16
Dec. 16, 2000	Leonids	0.18	Jun. 26, 2003	Germinids	0.05	Dec. 15, 2005	Geminids	0.06

9.2 Wild-2 Encounter

From the second Phase D dust model (Ray Newburn, private communication) we have calculated expected cumulative counting rates vs time from closest approach, and cumulative particle fluence for the DFMI PVDF sensors.

Figure 15 shows the calculated counting rates vs time from closest approach for the 20 cm^2 and 200 cm^2 PVDF sensors and **Figure 16** shows the same data at an expanded time scale for the 20 cm^2 sensor. Clearly, the 150 km flyby distance results in a period during which most of the data will be collected of only a few minutes.

In **Figure 17**, we show calculations of cumulative particle flux at closest approach (C.A.) vs particle mass m (g) for the PVDF sensors, and **Figure 18** shows calculations of cumulative particle fluence. For each figure, the particle mass thresholds are indicated for each PVDF sensor to illustrate the overlap in mass range.

In **Figure 19**, calculated values of cumulative counts measured vs time from closest approach for each PVDF sensor are presented. The flat portion of the curves corresponds to the data given in **Figure 18**.

In **Table 7** we show calculated tabulations of DFMI PVDF sensor counting rates at Wild-2 closest approach, and cumulative particle fluence.

For typical models of dust emission from the comet, similar calculations have been carried out by the U.K. group to predict possible results to be obtained from the DASS during the various flyby scenarios (McDonnell *et al.*, 1999).

Table 7

Expected DFMI PVDF Sensor Counting Rates At Wild-2 Closest Approach
(Based on the Second Phase D [Aug. 26, 1997] Dust Model -*Ray Newburn, Private Communication*)

20 cm^2 Sensor Cumulative Counting Rates (s^{-1})		200 cm^2 Sensor Cumulative Counting Rates (s^{-1})	
m_1 (> 9.8 x 10^{-12} g)	78	M_1 (> 8.5 x 10^{-8} g)	0.14
m_2 (> 1.2 x 10^{-10} g)	6.4	M_2 (> 1.7 x 10^{-6} g)	0.032
m_3 (> 4.3 x 10^{-9} g)	0.2	M_3 (> 1.4 x 10^{-5} g)	0.017
m_4 (> 6.3 x 10^{-7} g)	0.004	M_4 (> 1.5 x 10^{-4} g)	0.0048

Expected DFMI PVDF Sensor Cumulative Particle Fluence
(Based on the Second Phase D [Aug. 26, 1997] Dust Model -*Ray Newburn, Private Communication*)

20 cm^2 Sensor Cumulative Particle Fluence		200 cm^2 Sensor Cumulative Particle Fluence	
m_1 (> 9.8 x 10^{-12} g)	6000	M_1 (> 8.5 x 10^{-8} g)	11
m_2 (> 1.2 x 10^{-10} g)	493	M_2 (> 1.7 x 10^{-6} g)	2.5
m_3 (> 4.3 x 10^{-9} g)	14	M_3 (> 1.4 x 10^{-5} g)	1.3
m_4 (> 6.3 x 10^{-7} g)	0.3	M_4 (> 1.5 x 10^{-4} g)	0.4

10.0 ACKNOWLEDGEMENTS

We wish to thank Noel Hinners for his efforts which led to inclusion of the DFMI instrument as part of the *STARDUST* payload, and Dave Perkins, Allan Cheuvront, Tom Duxbury, Chuck

Action and Howard Taylor for their efforts related to DFMI spacecraft integration and data acquisition by the spacecraft. Ray Newburn kindly provided his Phase D dust model results, which served as the basis for the PVDF sensor calculations given in Section 9.2. Finally, we thank F. DiDonna and P. DiDonna for their important contributions to the design, construction, testing, and calibration of the DFMI, Ellen Larue for constructing the DFMI PVDF sensors, Fred Hörz for carrying out particle penetration measurements on cooled PVDF sensors, the Aerospace Corp. for their assistance in evaluation of thermal design of the sensors, and E. Grün and E. Igenbergs for making our Heidelberg and Munich calibrations possible. The University of Chicago effort was supported by LMA Contract RF6-457089. The group at the University of Kent acknowledges receipt of a grant from PPARC (UK).

10. REFERENCES

Anderson et al.: 1999, this issue.

Burchell M.J., Cole M.J., McDonnell J.A.M. and Zarnecki J.C., 1999, "Hypervelocity Impact Studies Using the 2 MV Van de Graaff Accelerator and Two-Stage Light Gas Gun of the University of Kent at Canterbury", *Meas. Sci. Technol.* **10**, 41-50.

Brownlee et al.: 1999, this issue.

Cook, A.F.: 1973, in Evolutionary and Physical Properties of Meteoroids, IAU, Col. 13, 183, NASA SP-319.

deNolfo, G., Simpson, J.A., Tuzzolino, A.J., Ksanfomality, L.V. and Sagdeev, R.Z.: 1991, "Detection of Micron-Sized Particles in Meteor Streams Crossing the Trajectories of the VEGA-1 and VEGA-2 Spacecraft", *Lunar and Planetary Science* **XX11**, 313.

Duxbury et al.: 1999, this issue.

Grün, E., et al.: 1993, "Discovery of Jovian Dust Streams and Interstellar Grains by the Ulysses Spacecraft", *Nature*, **362**, 428.

Kissel et al.: 1999, this issue.

McDonnell J.A.M., 1969, "Calibration Studies on a Piezoelectric Sensing Diaphragm for the Detection of Micrometeorites in Space", *J. Sci. Instruments (J. Phys. E)* **2**, 1026-1030.

McDonnell J.A.M. and Abellanas C., 1972, "A Technique for Position Sensing and Improved Momentum Evaluation of Microparticle Impacts In Space", *Rev., Sci. Inst.*, **43**, 1214-1216.

McDonnell J.A.M. *et al.*, 1986, "Dust Density and Mass Distribution Near Comet Halley from Giotto Observations", *Nature* **321**, 338-340.

McDonnell J.A.M. *et al.*, 1999, "The Stardust Dust Flux Monitor", to appear in Adv. in Space Research.

Newburn et al.: 1999, this issue.

Perkins, M.A. Simpson, J.A. and Tuzzolino, A.J.: 1985, "A Cometary and Interplanetary Dust Experiment on the VEGA spacecraft missions to Halley's Comet", *Nucl. Instr. and Meth.* **A239**, 310.

Simpson, J.A. and Tuzzolino, A.J.: 1985, "Polarized Polymer Films as Electronic Pulse Detectors of Cosmic Dust Particles, *Nucl. Instr. and Meths.* **A236**, 187.

Simpson et al.: 1986, "Dust Counter and Mass Analyzer (DUCMA) Measurements of Comet Halley's Coma From *Vega* Spacecraft', *Nature* **321**, 278.

Simpson, J.A., Rabinowitz, D. and Tuzzolino, A.J.: 1989, "Cosmic Dust Investigations: I, PVDF Detector Signal Dependence on Mass and Velocity for Penetrating Particles", *Nucl. Instr. and Meths.* **A279**, 611.

Singer, S.F. and Stanley, J.E.: 1980, in Solid Particles in the Solar System (I. Halliday and B.A. McIntosh, eds.) D. Reidel, Boston, 329.

Tsou et al.: 1999, this issue.

Tuzzolino, A.J.: 1996, "Applications of PVDF Dust Sensor Systems in Space," *Adv. Space Res.*, **Vol. 17**, Number 12, 123.

Tuzzolino, A.J.: 1998, "The High Rate Detector Component of the Cosmic Dust Analyzer (CDA)", to appear in *Space Science Reviews*, 1999.

a)

THE UNIVERSITY OF CHICAGO DUST FLUX MONITOR INSTRUMENT (DFMI) FOR THE STARDUST MISSION

DFMI CHARACTERISTICS

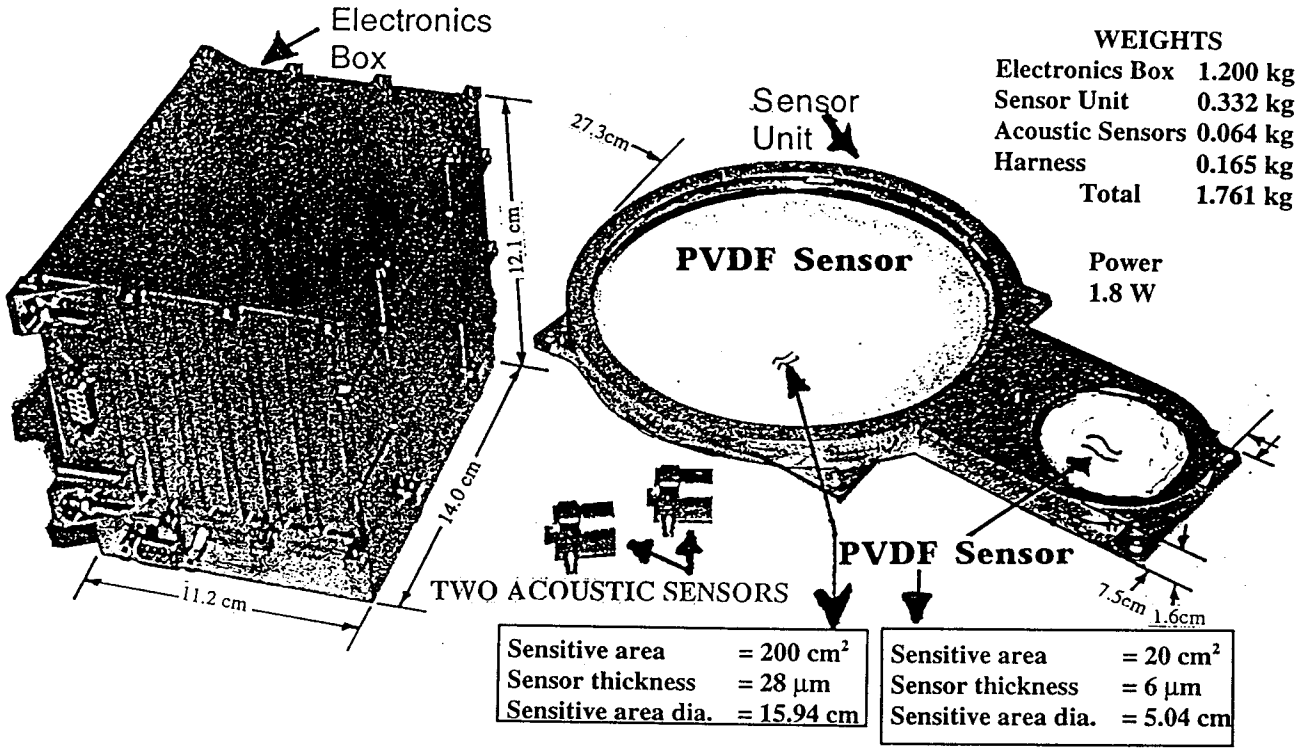

WEIGHTS

Electronics Box	1.200 kg
Sensor Unit	0.332 kg
Acoustic Sensors	0.064 kg
Harness	0.165 kg
Total	1.761 kg

Power
1.8 W

Sensitive area	= 200 cm²
Sensor thickness	= 28 μm
Sensitive area dia.	= 15.94 cm

Sensitive area	= 20 cm²
Sensor thickness	= 6 μm
Sensitive area dia.	= 5.04 cm

b)

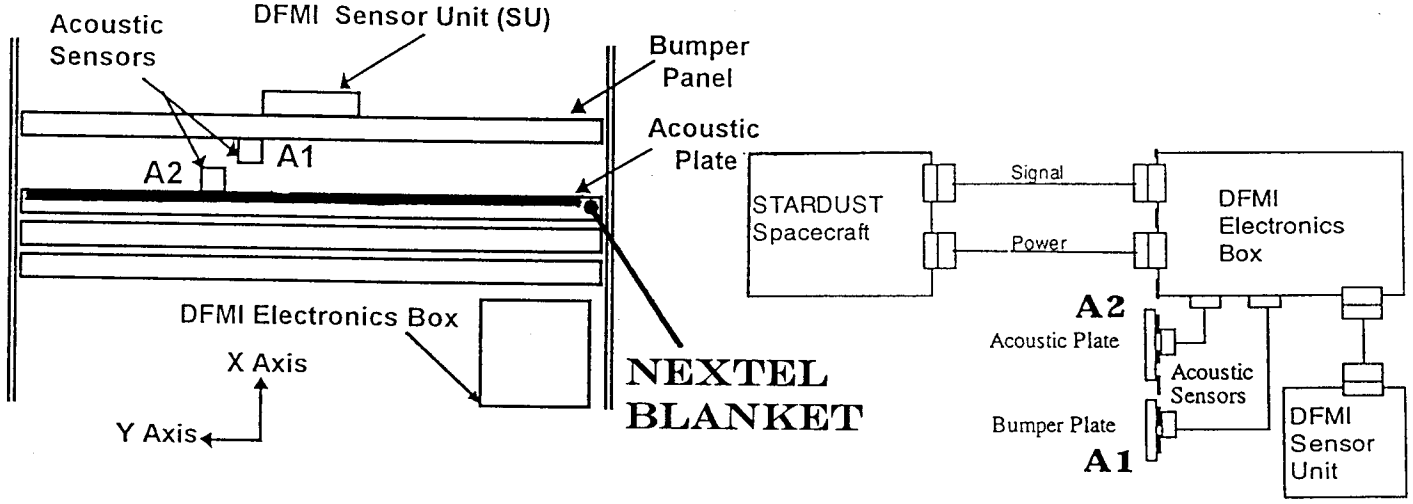

DFMI CHARACTERISTICS

PVDF Sensors:	200 cm², 28μm thick; 20 cm², 6μm.
Acoustic Sensors:	Two identical Quartz piezoelectric accelerometers.
Thresholds:	Each PVDF sensor has four mass thresholds and each acoustic sensor has two mass thresholds.
Particle Mass:	For PVDF sensors at 6.1 km/s impact velocity, differential and integral flux ~ 10^{-11} g to 10^{-4} g; integral flux > 10^{-4} g.
Counting Rates:	(PVDF SENSORS): Up to 10^4 s^{-1}, < 5% corrections; 10^4 to 10^5 s^{-1}, known correction

Figure 1. a) Photograph of the DFMI;
b) Schematic layout of the DFMI SU, EB and acoustic sensors on the spacecraft.

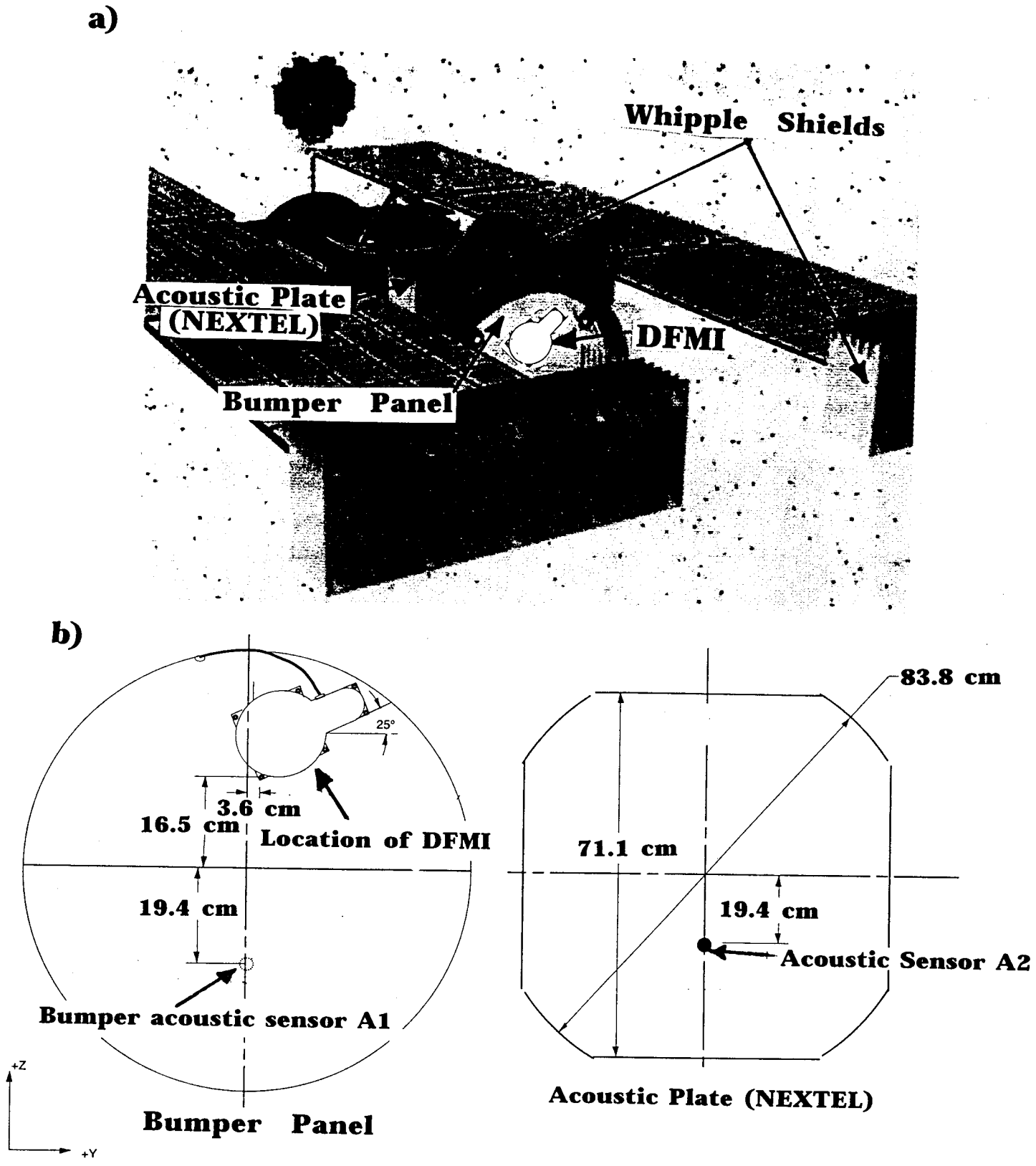

Figure 2. **a)** Schematic of the *Stardust* spacecraft showing the location of the PVDF DUST SENSOR UNIT (SU);
b) Location of the DFMI SU and acoustic sensor A1 on the Bumper panel. Acoustic sensor A1 is mounted to the underside of the Bumper panel;
c) Location of acoustic sensor A2 on the Acoustic (NEXTEL) plate.

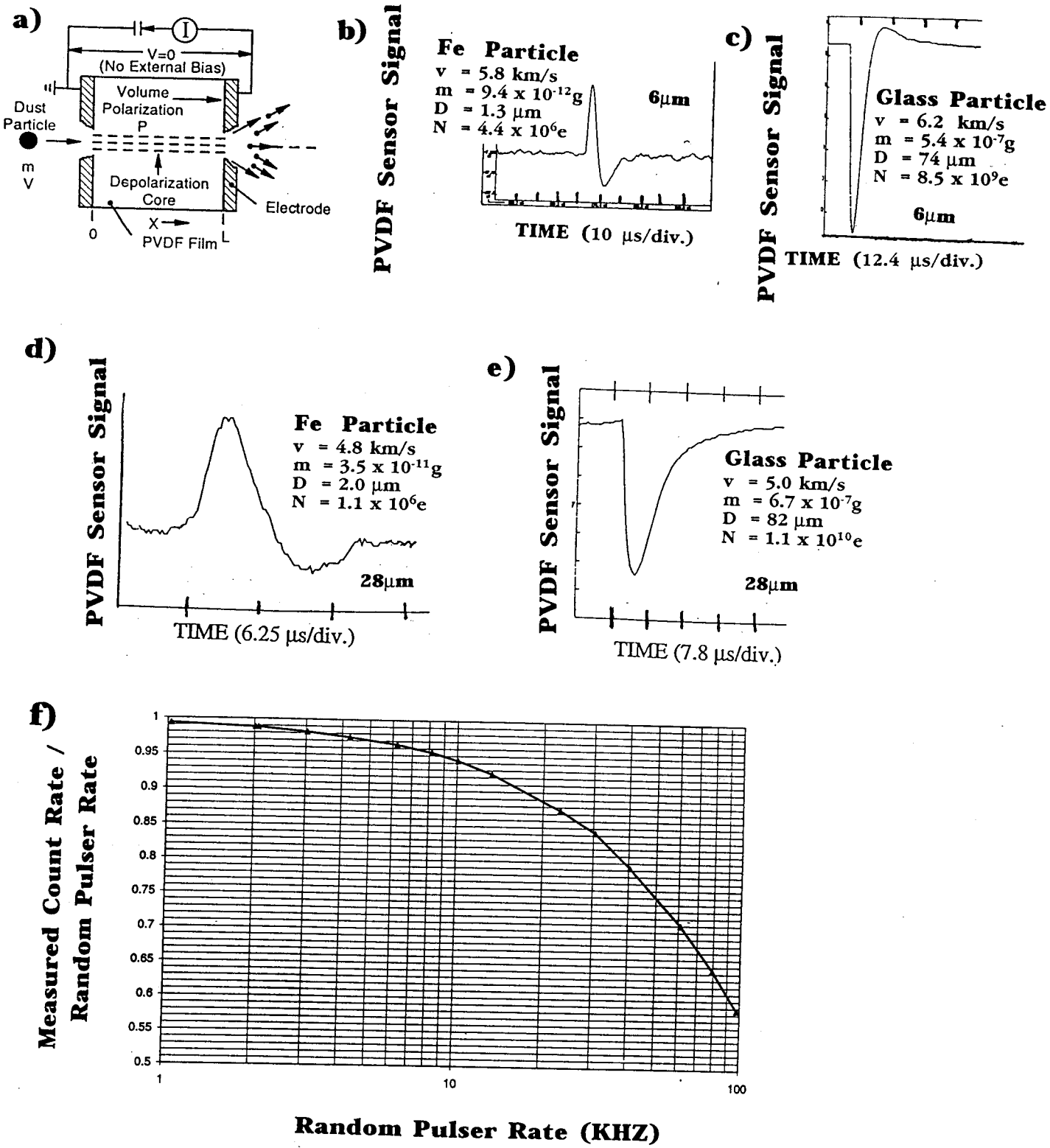

Figure 3. **a)** Schematic of a polarized PVDF sample with conducting contact electrodes. An incident particle of mass m and impact velocity v penetrates (or stops within) the PVDF sample resulting in complete local depolarization along its track;

b) and **c)** Examples of output signals from a 6 μm thick PVDF sensor;

d) and **e)** Examples of output signals from a 28 μm thick PVDF sensor; For panels "b)-e)", listed are particle velocity, mass, diameter, and output signal amplitude expressed in units of numbers of electron charges;

f) Ratio of measured counting frequency to random pulser frequency vs random pulser frequency.

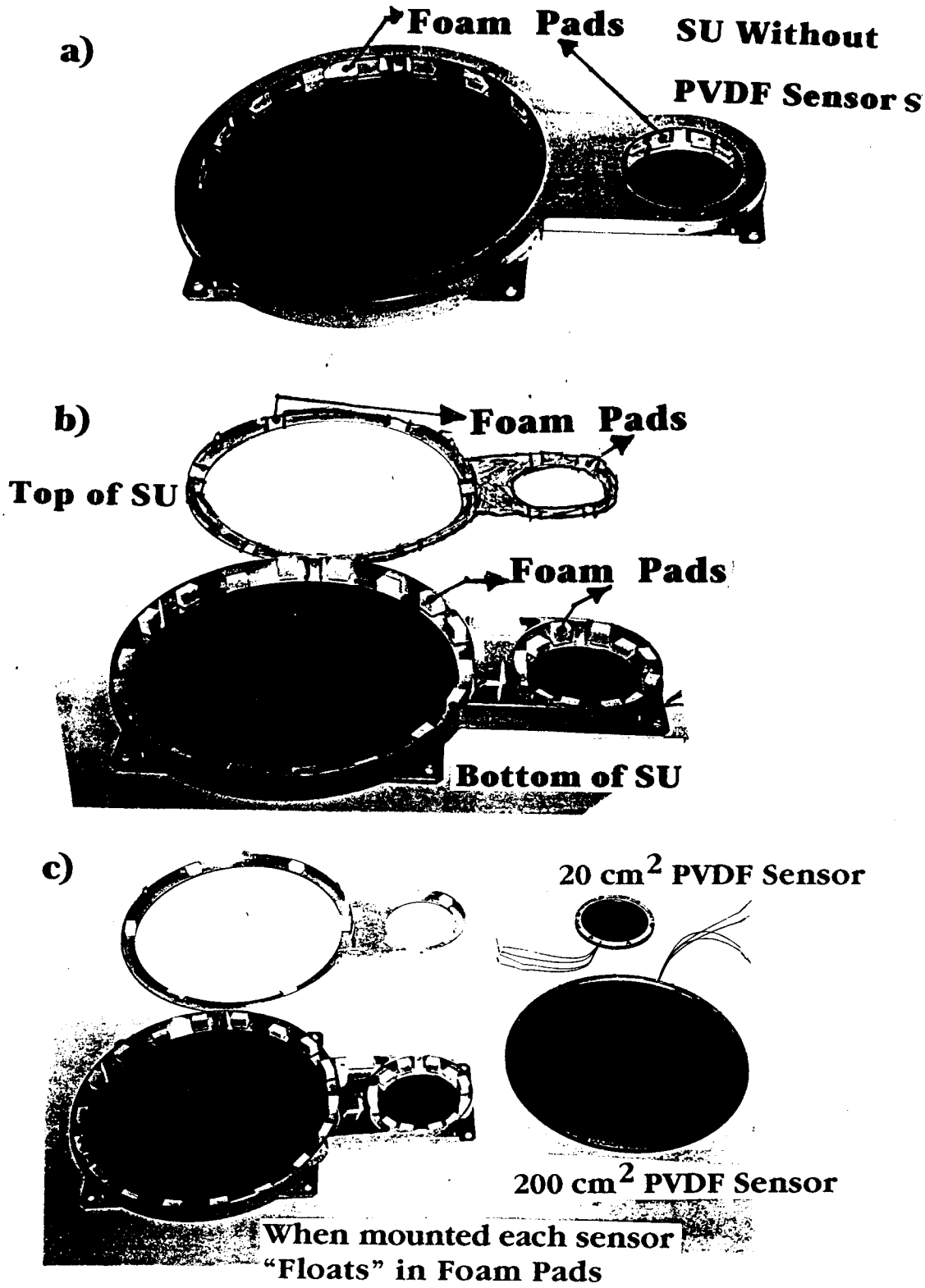

Figure 4. **a)** Photograph of the DFMI SU with no PVDF sensors mounted to show the arrangement of foam pads attached to the inner circular surfaces of the SU;
b) Top cover of SU removed to again show the arrangement of foam pads;
c) When the PVDF sensors are mounted into the SU enclosures, each sensor "floats" in the foam pad arrangements.

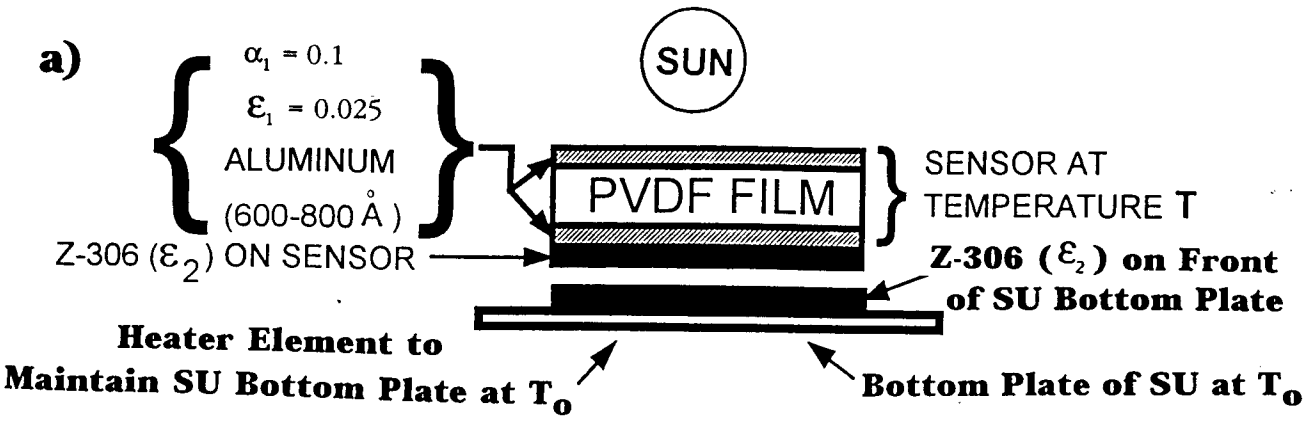

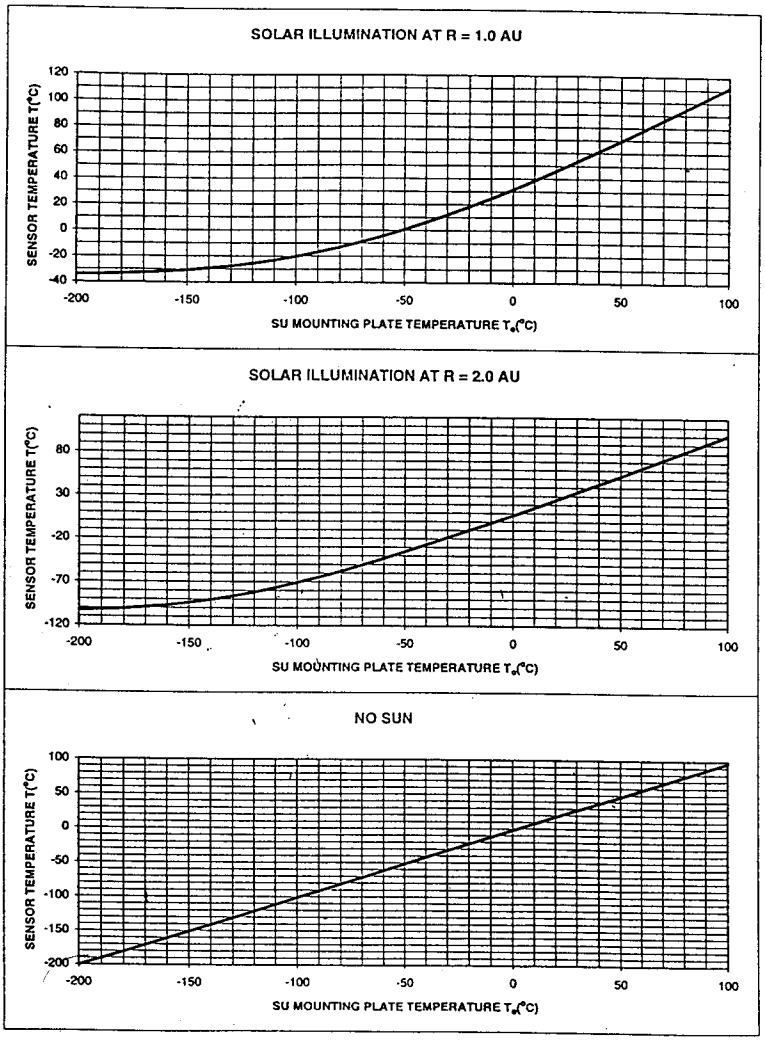

Figure 5. a) Thermal mode assumed for the DFMI dust sensors. The space-viewing sensor surface (front) either views the Sun (normal incidence), or is in the dark (no-Sun condition). The sensor front surface has absorptivity, α_1 = 0.1, and emissivity ε_1 = 0.025. The back surface of the sensor is coated with Z-306 (ε_2 = 0.84) and is close to a Z-306 coating (ε_2 = 0.84), which has been applied to the upper surface of the SU bottom place. The sensor is a temperature T and the bottom plate of the SU is maintained at temperature T_o;

b-d) Calculated sensor temperature T vs assumed values for T_o for the model shown in "a)"; b) Sensor solar illumination at 1.0 AU; c) Sensor solar illumination at 2.0 AU; d) No sensor solar illumination.

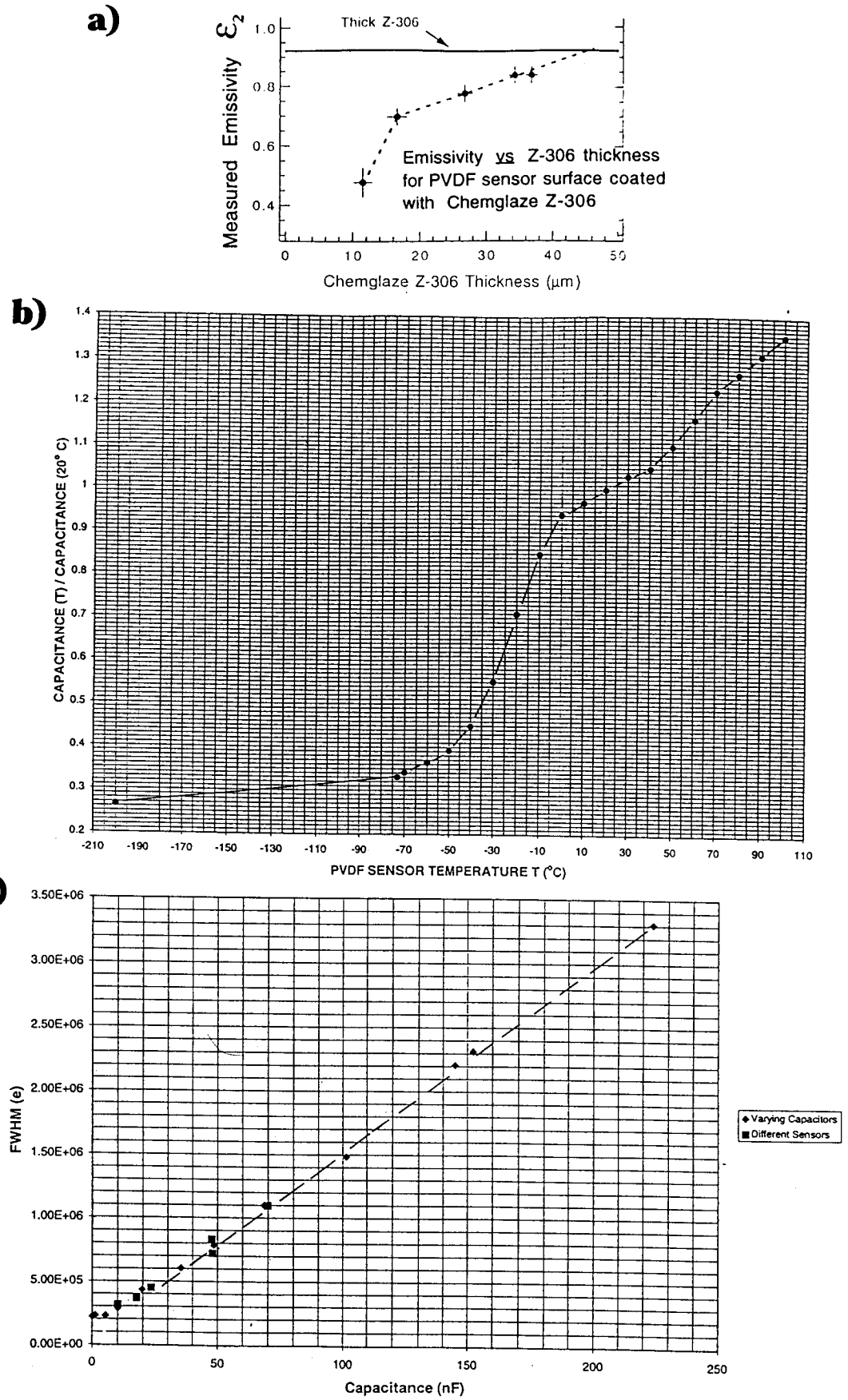

Figure 6. **a)** Measured emissivity ε_2 vs Chemglaze Z-306 thickness (μm);
b) Ratio of measured sensor capacitance at temperature T to sensor capacitance at 20°C vs PVDF sensor temperature T;
c) Measured electronic noise (FWHM) expressed in units of number of electrons (e) at the input to the DFMI PVDF sensor charge sensitive preamplifier (CSA) vs sensor capacitance.

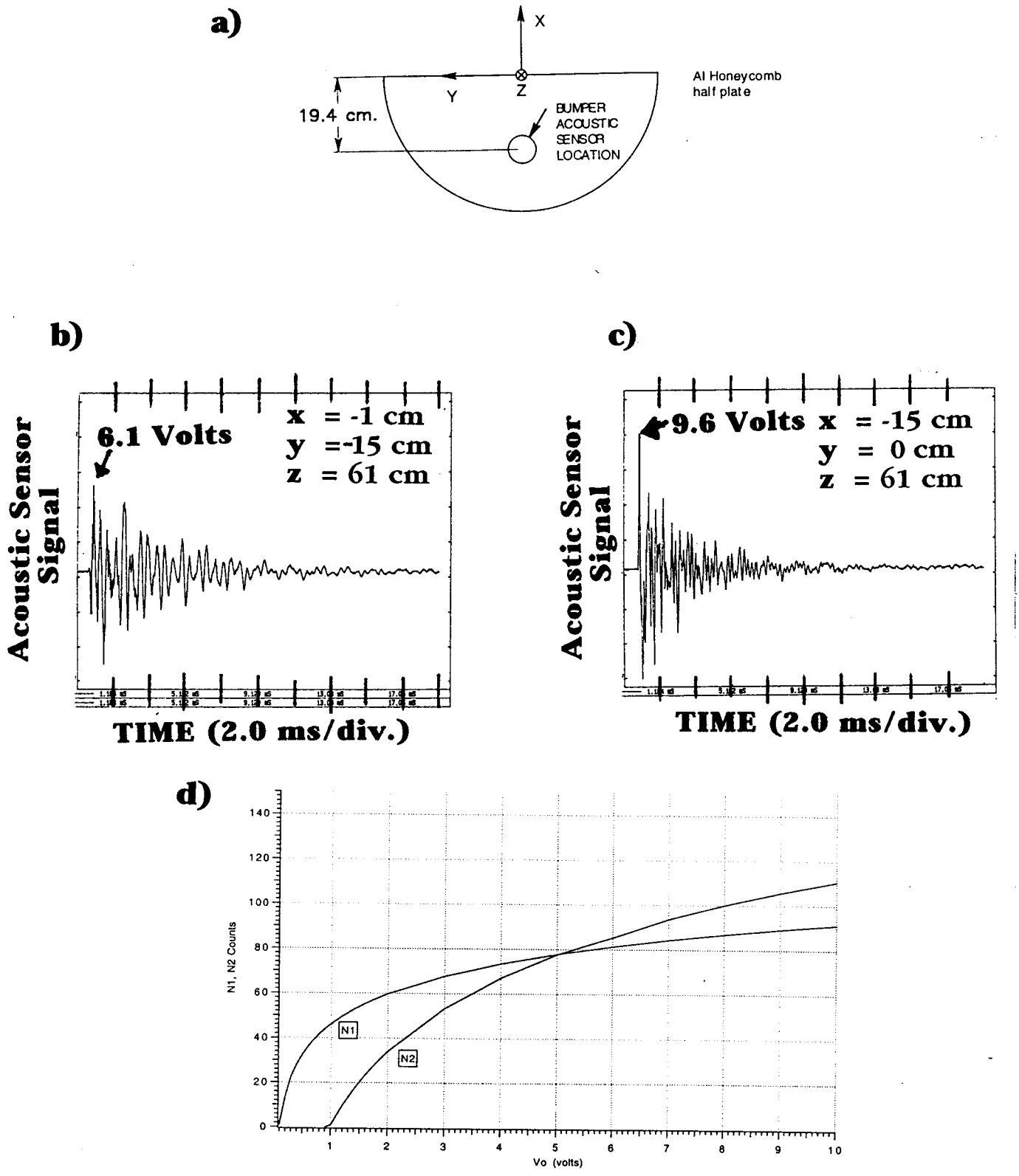

Figure 7. a) Location of the Bumper acoustic sensor on the Bumper plate. The axes serve to indicate the impact coordinates on the plate (x,y) when a 0.47 g aluminum sphere is dropped from a height Z above the Bumper plate surface;

b) and **c)** Examples of output signals from the Bumper acoustic sensor for two different impact points on the Bumper panel;

d) Calculated N1, N2 counts (from Eq. 6) vs V_0 for the case where $T_1 >> \Delta t$.

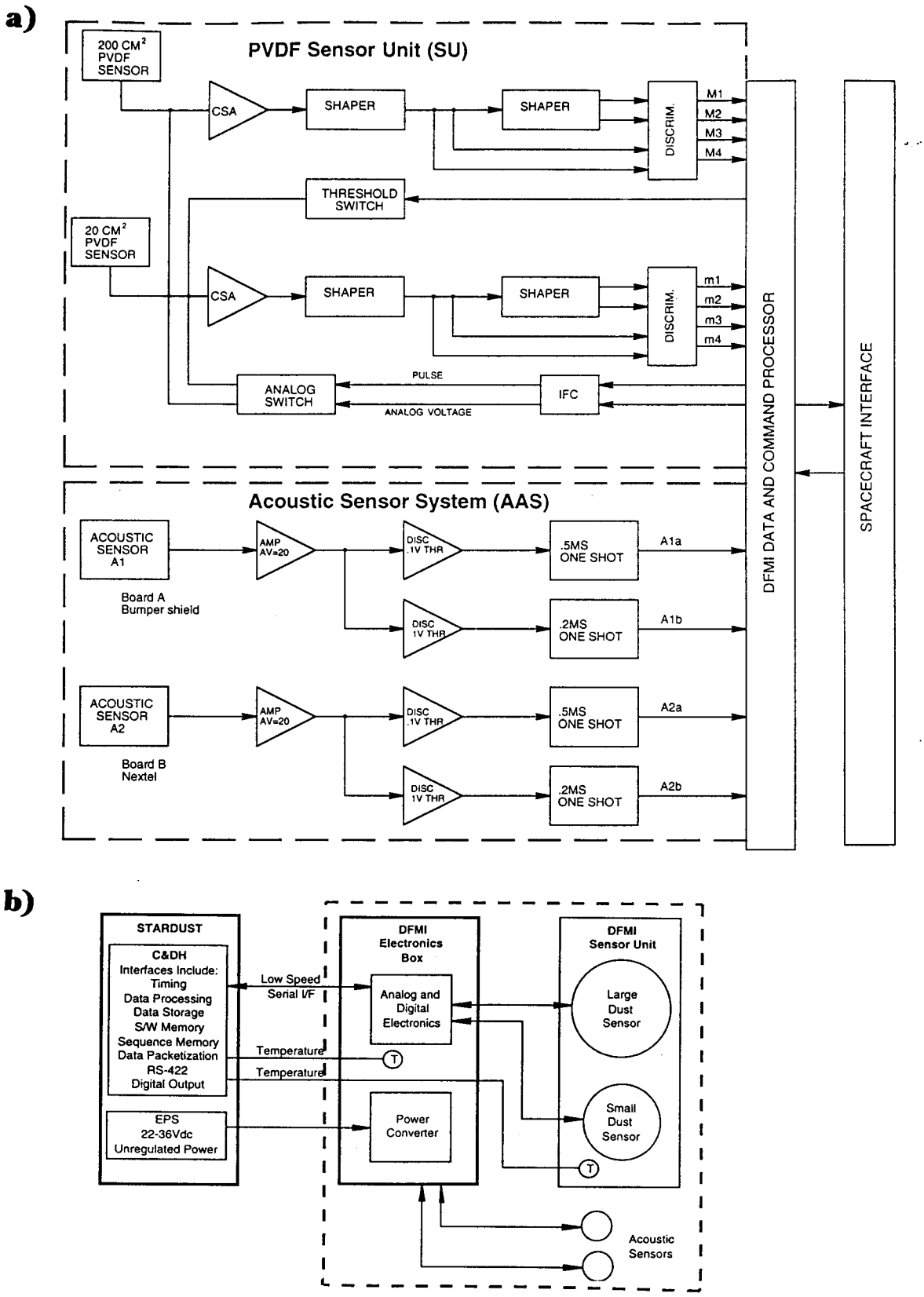

Figure 8. **a)** Block diagram of the principal electronic functions of the DFMI; **b)** Schematic of the DFMI-spacecraft electrical interface.

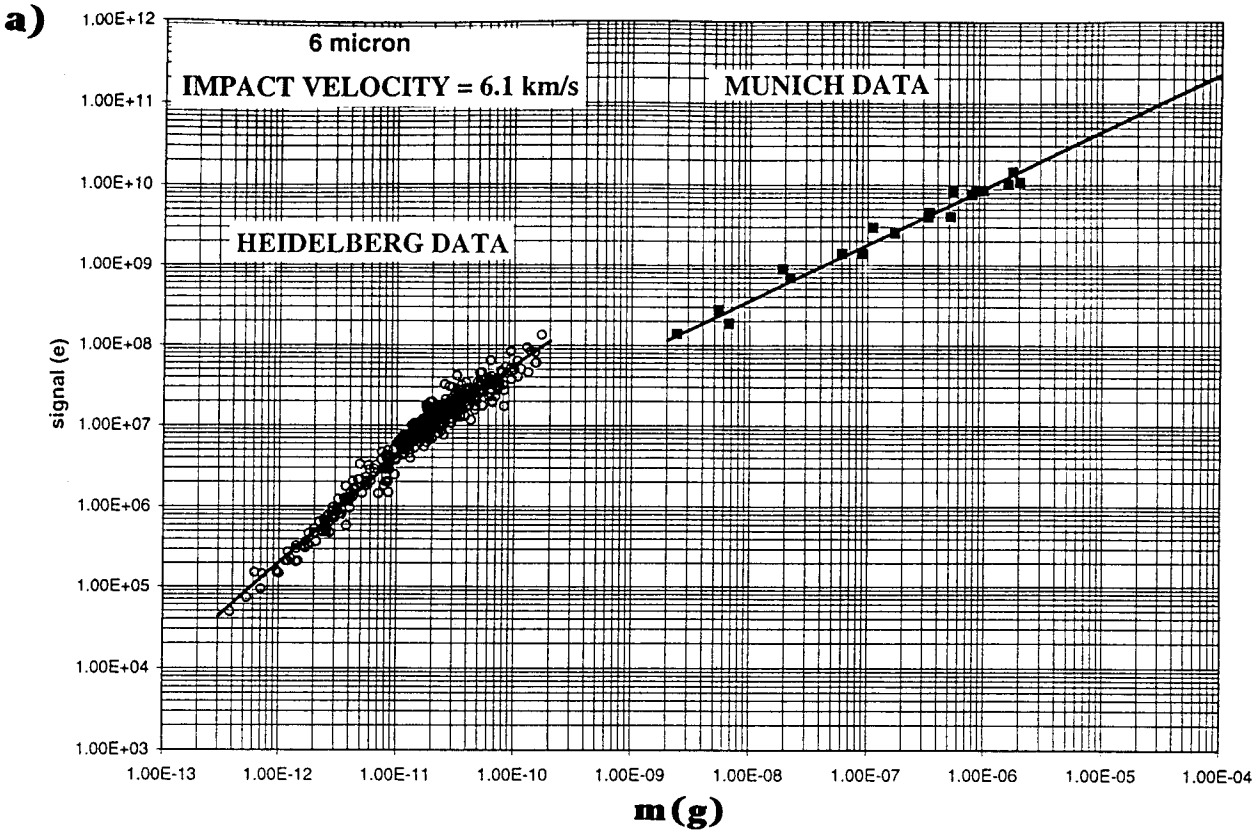

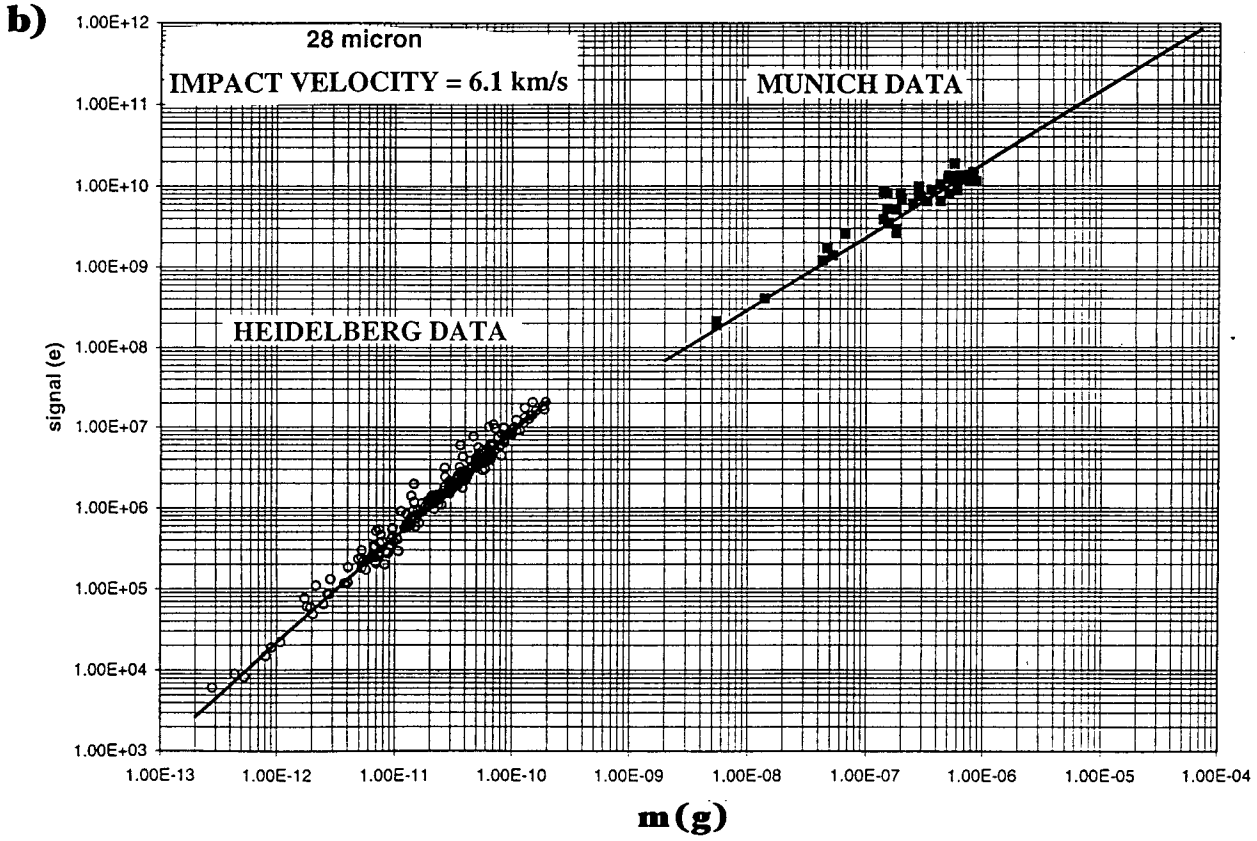

Figure 9. **a)** PVDF sensor output signal vs particle mass m(g) for a 6 μm thick sensor impacted by particles with impact velocity = 6.1 km/s;
b) PVDF sensor output signal vs particle mass m(g) for a 28 μm thick sensor impacted by particles with impact velocity 6.1 km/s.

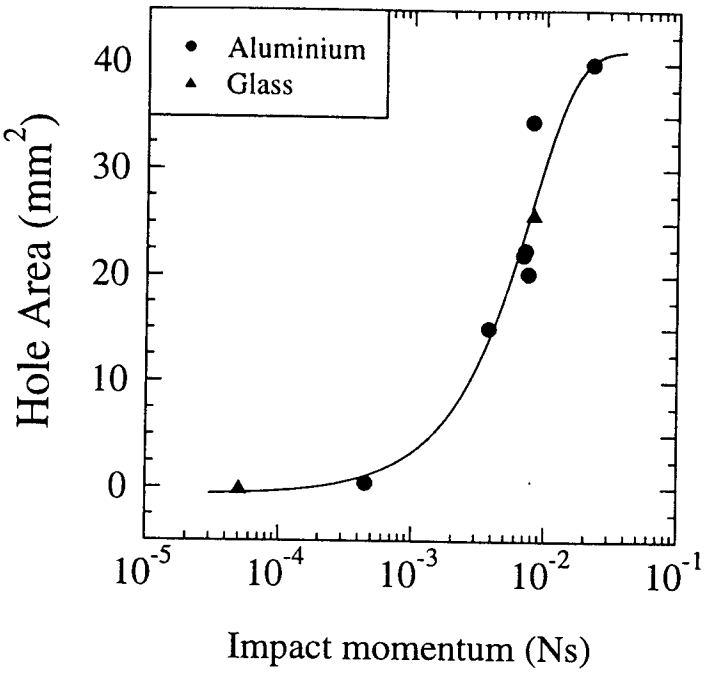

Figure 10. Bumpershield rear surface hole area vs. impactor momemtum for hypervelocity impacts (see text for details of the fit).

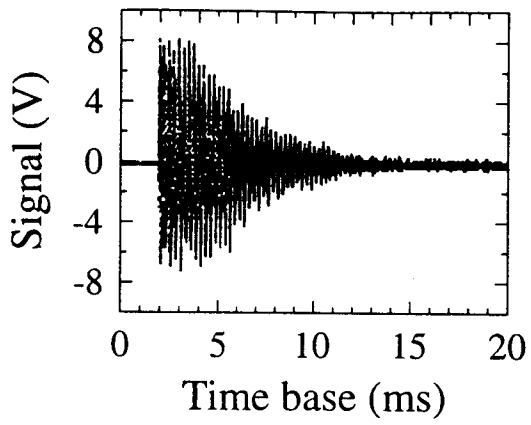

Figure 11. Bumpershield acoustic sensor output signal for the impact of a 1 mm glass sphere at 6.1 kms^{-1}, 4 cm from the sensor.

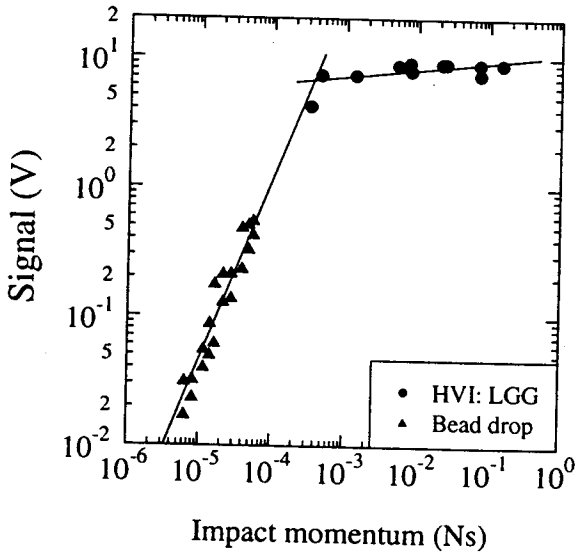

Figure 12. Bumpershield acoustic sensor signal strenght vs. impact momentum for impacts 5 cm from the sensor. The influence of the ballistic limit for penetration is clearly evident. (See text for details of fit).

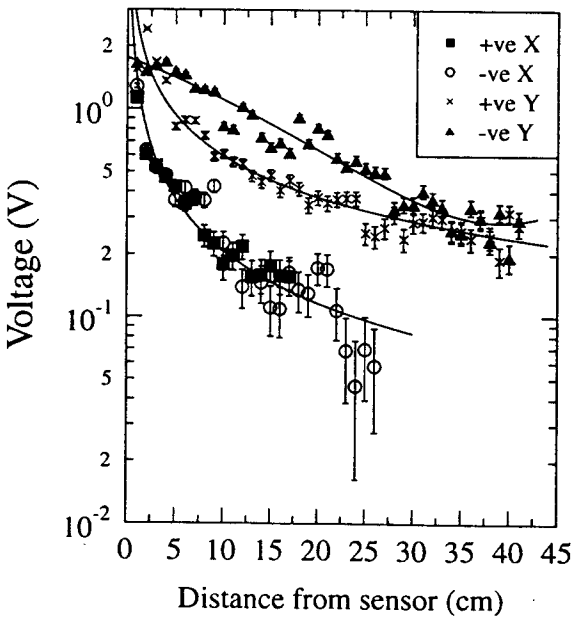

Figure 13. Bumpershield acoustic sensor signal strenght vs. impact distance from the sensor (for bead drops of momentyum 2.4 x 10^{-5} N s). The data are used to generate an effective area for the bumpershield under a distribution of impact masses. (See text for details of the fits).

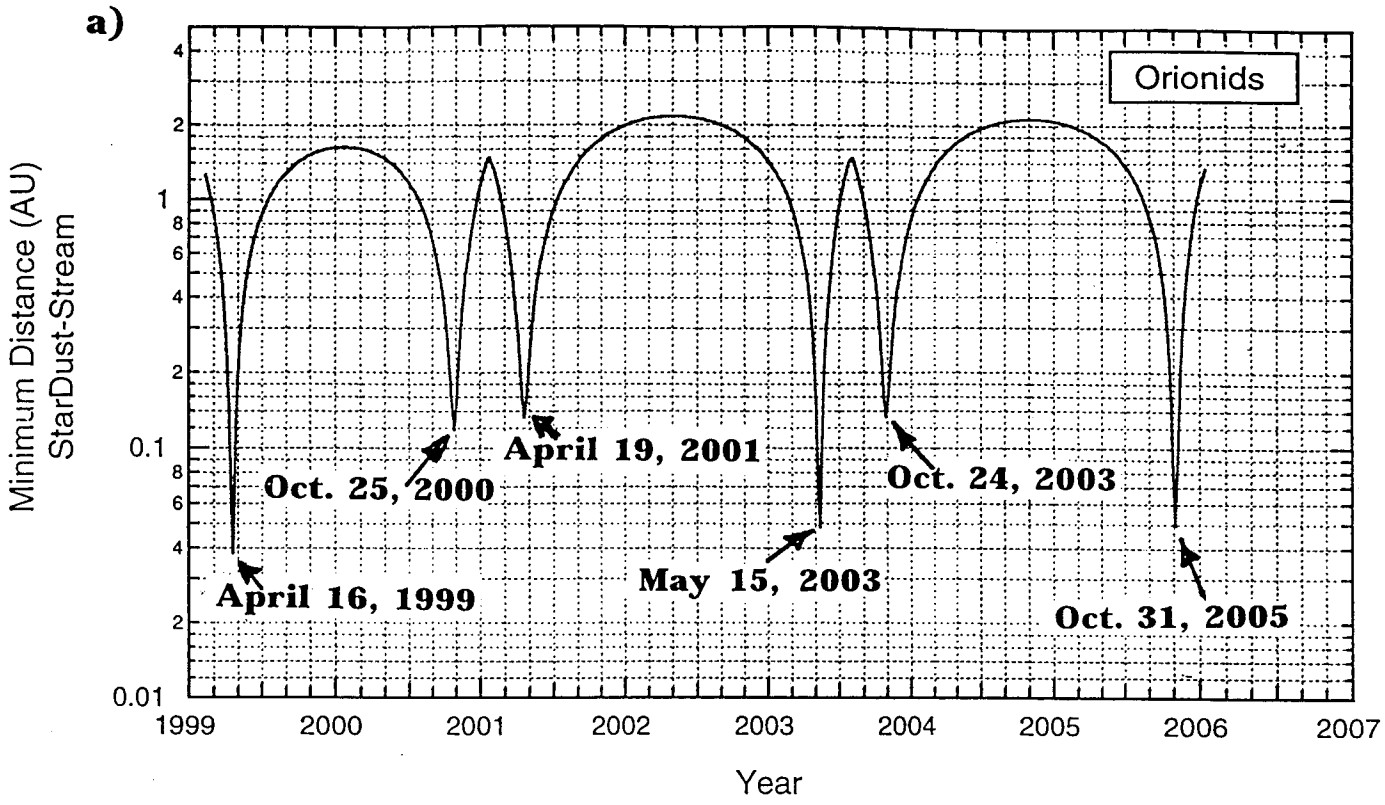

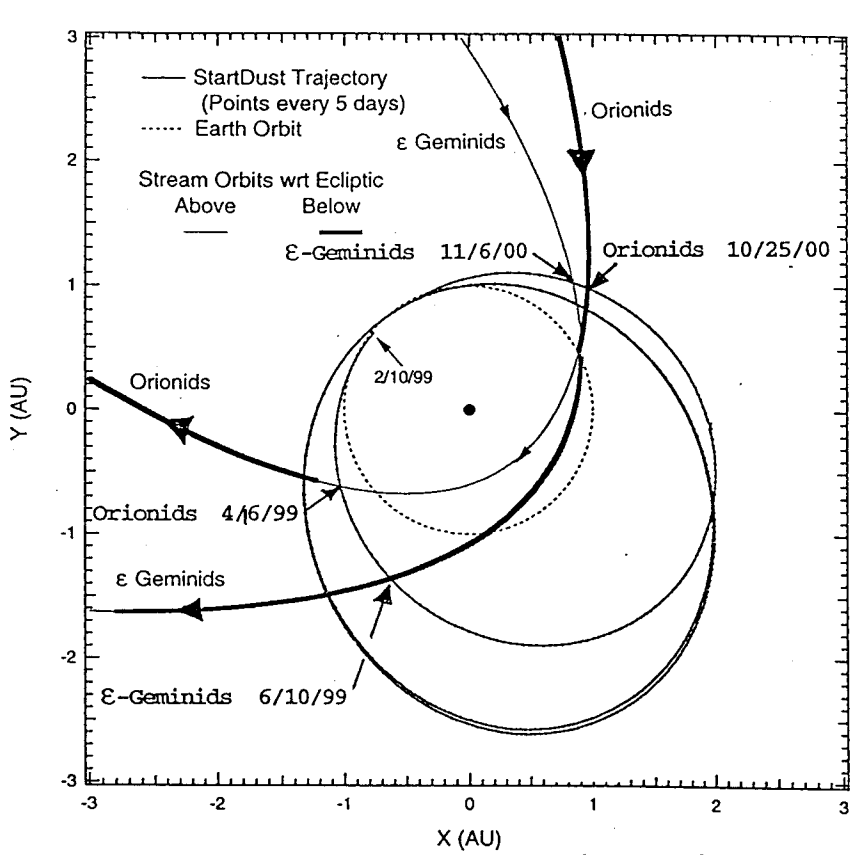

Figure 14.a) Minimum separation distance between the *Stardust* spacecraft and meteor stream trajectory for the case of the Orionids meteor stream. Indicated are dates corresponding to the minima in the curse;

b) Projected trajectories of the *Stardust* spacecraft and the ε-Geminids and Orionids meteor streams. The Sun is at the origin and the **x,y** plane is the ecliptic plane, with the **x** axis pointing to the Vernal Equinox (γ). Indicated are the minimum SPACECRAFT/METEOR-STREAM separations for the first loop of the *Stardust* spacecraft.

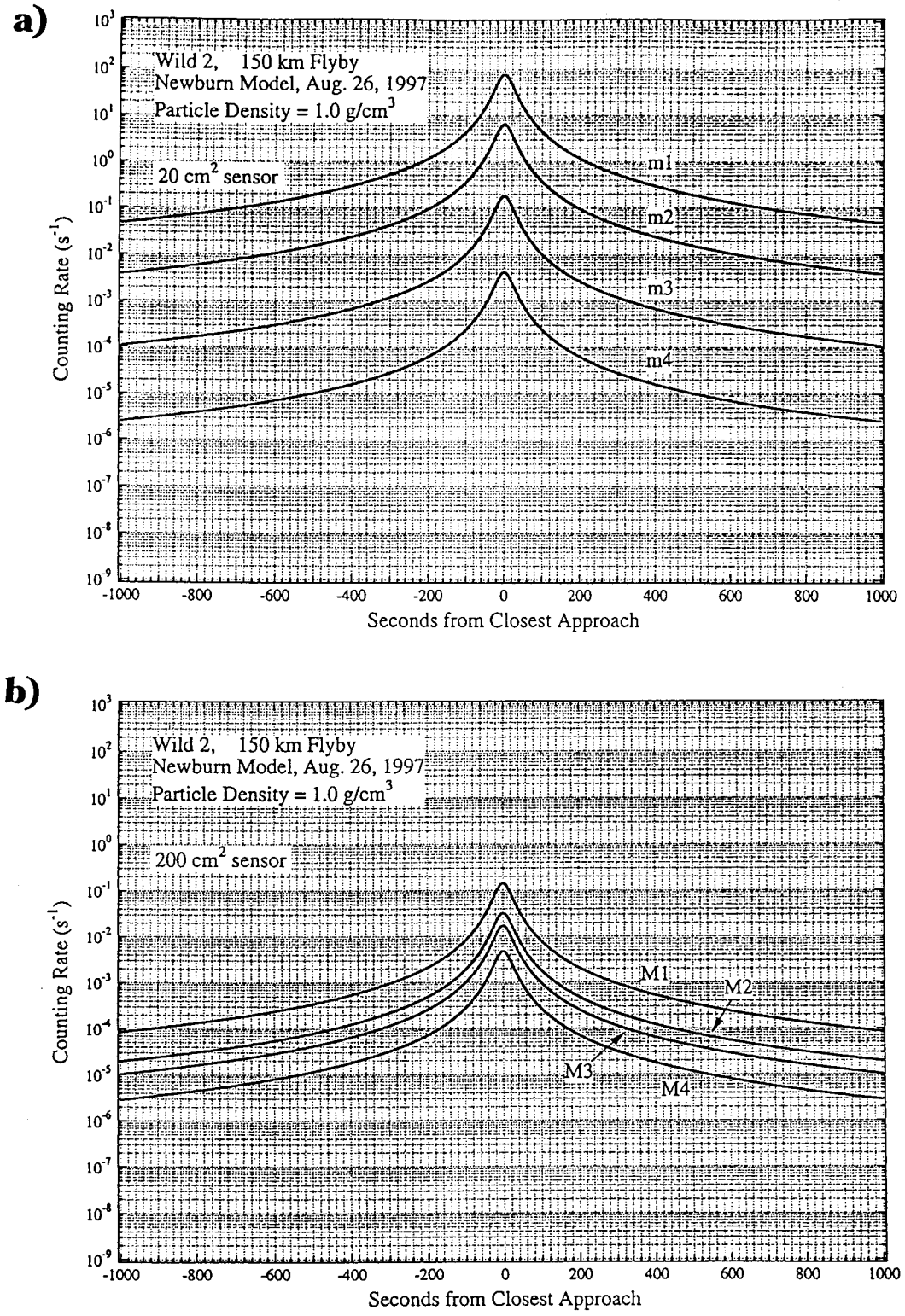

Figure 15. Calculated counting rates vs time from WILD-2 closest approach based on the Newburn second phase D dust model:

a) Calculations for the 20 cm^2 DFMI PVDF sensor;

b) Calculations for the 200 cm^2 DFMI PVDF sensor.

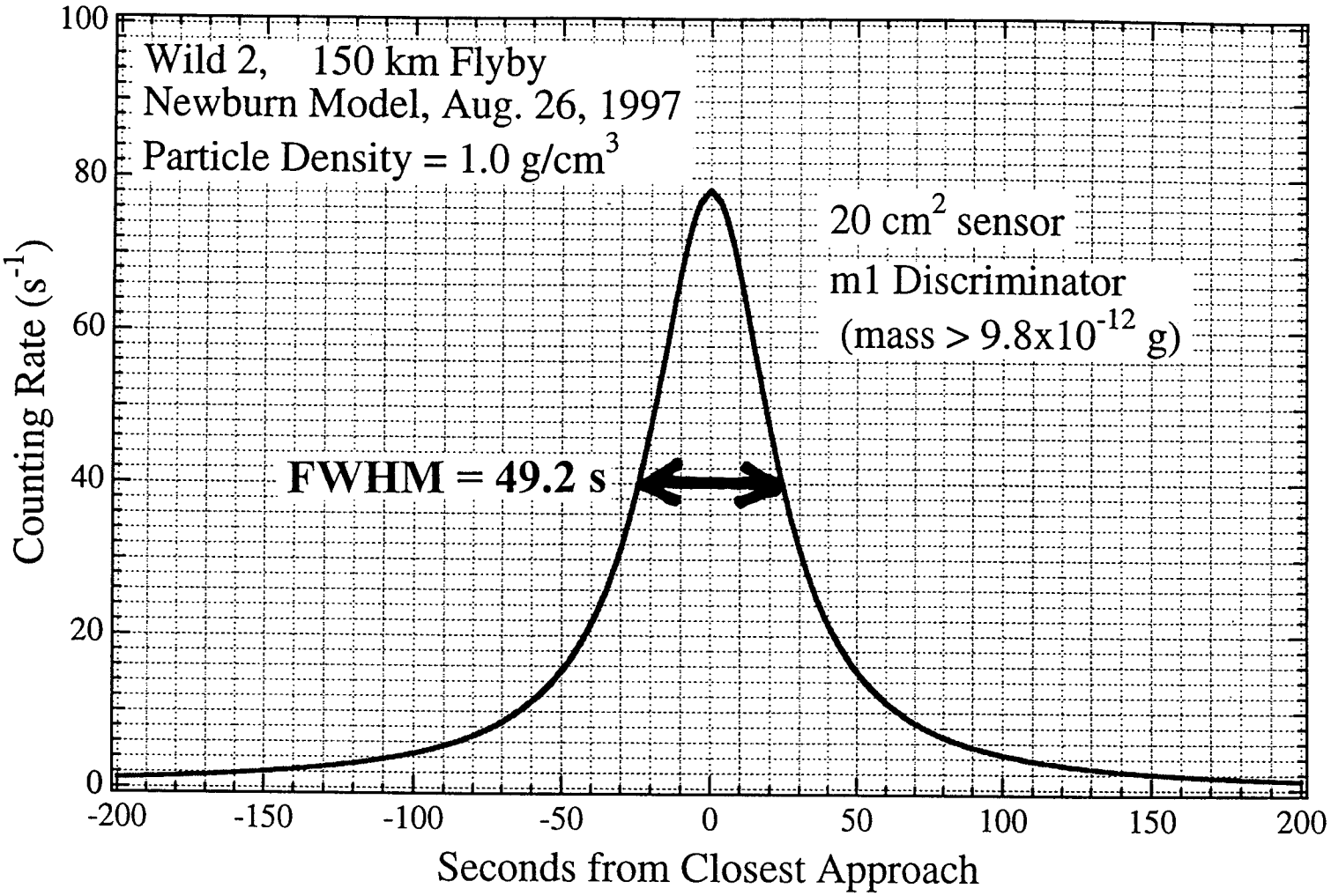

Figure 16. The data corresponding to the m1 curve in **Figure 15a**, but at higher time resolution.

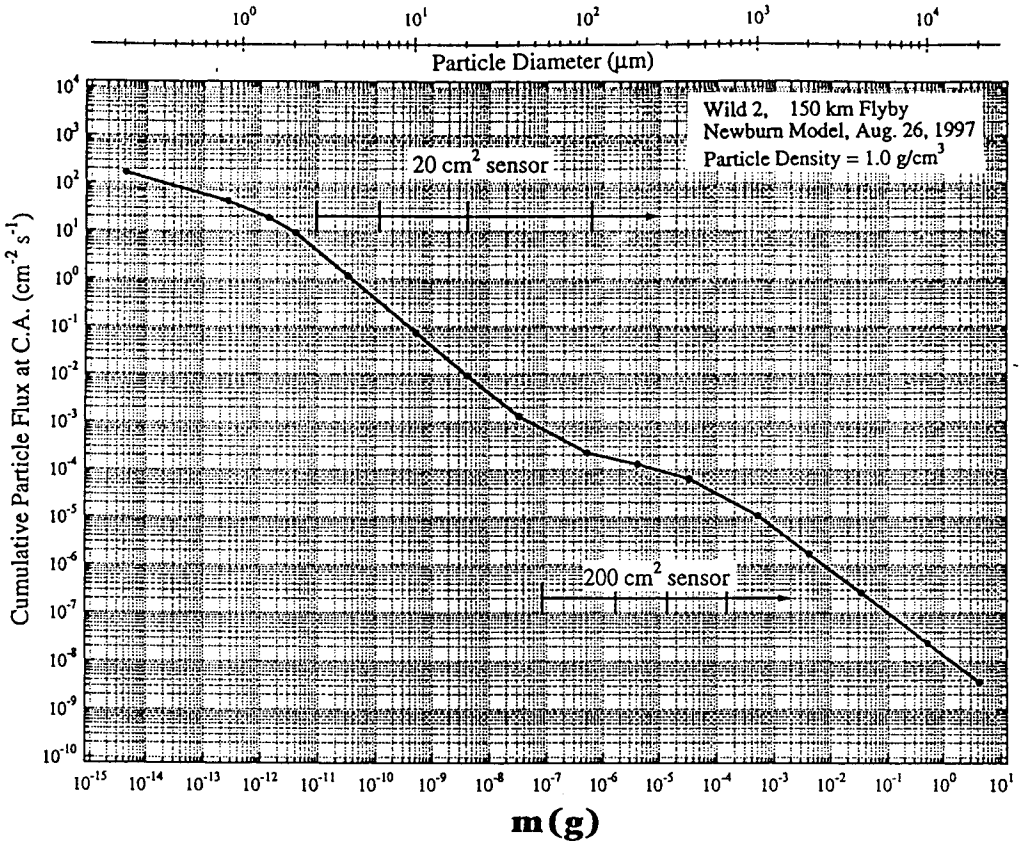

Figure 17. Calculated cumulative particle flux at WILD-2 closest approach (C.A.) vs. particle mass m(g) from the Newburn second Phase D dust model. The four mass thresholds for each of the two PVDF sensors are indicated by vertical bars.

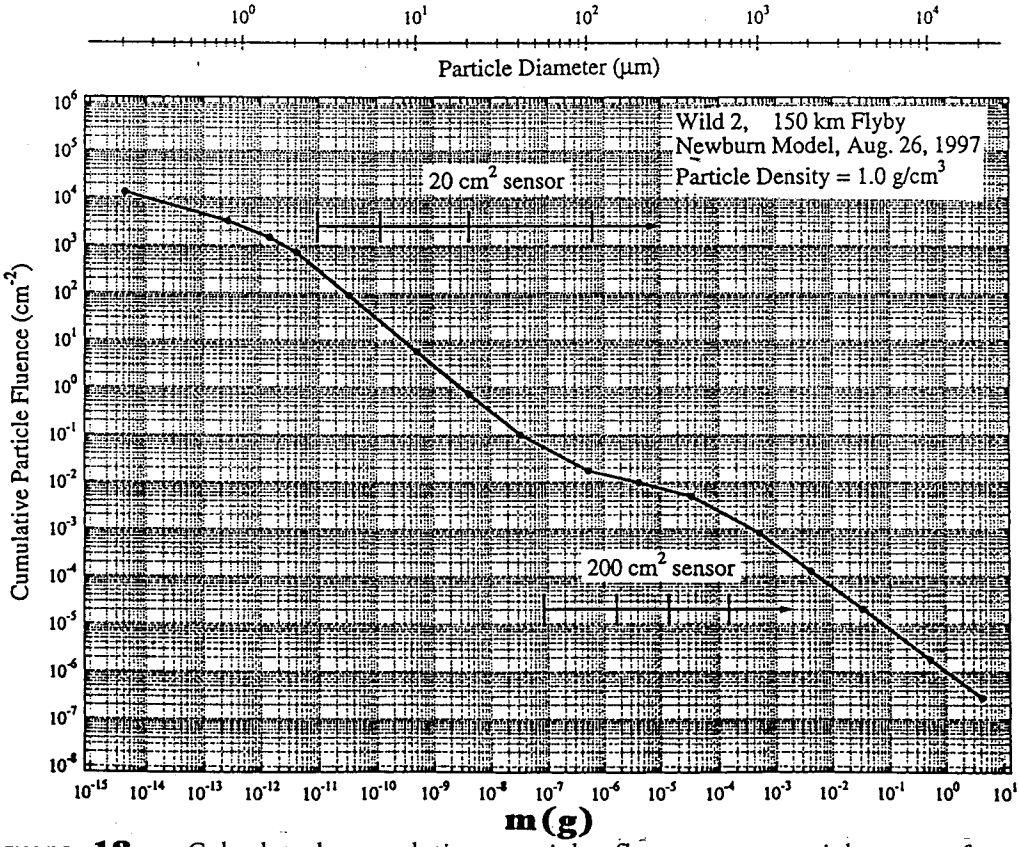

Figure 18. Calculated cumulative particle fluence vs particle mass from the Newburn second phase D dust model. The four mass thresholds for each of the two PVDF sensors are indicated by vertical bars.

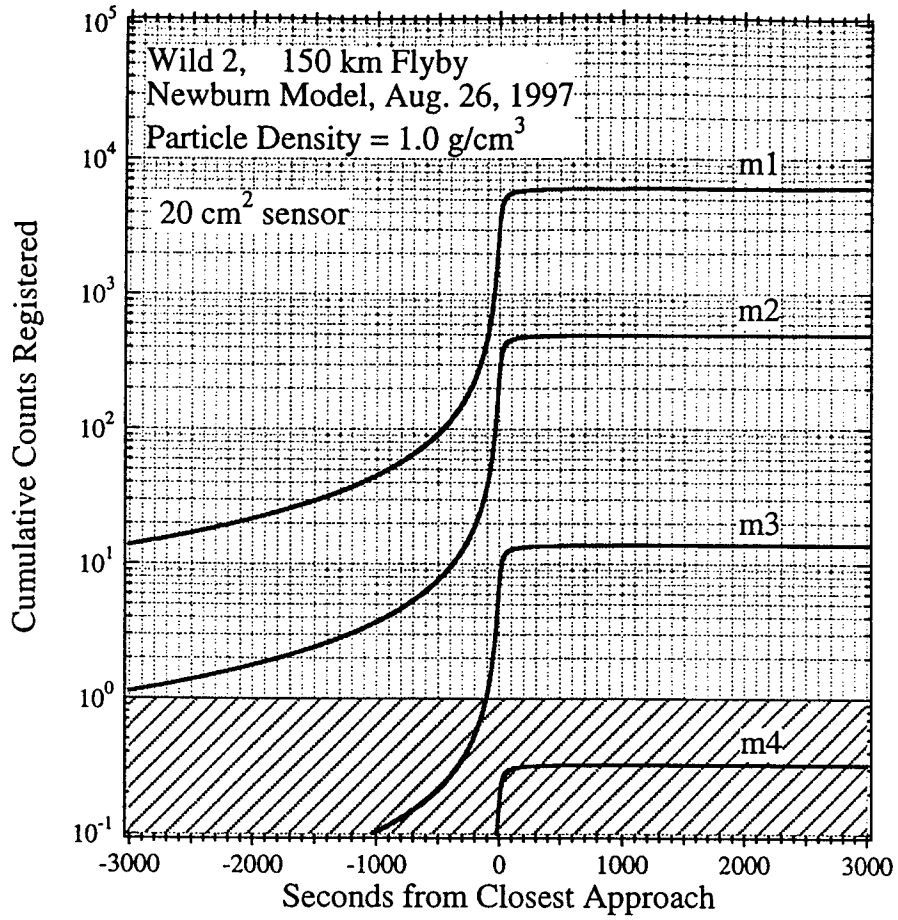

Figure 19. Calculations of cumulative counts registered vs seconds from closest approach:

a) Calculated data for the 20 cm^2 PVDF sensor;

b) Calculated data for the 200 cm^2 PVDF sensor.